# Real-time completion monitoring with acoustic waves

Andrey Bakulin[1], Alexander Sidorov[2], Boris Kashtan[2], and Mikko Jaaskelainen[1]

## ABSTRACT

Deepwater production is challenged by well underperformance issues that are hard to diagnose early on and expensive to deal with later. Problems are amplified by reliance on a few complex wells with sophisticated sand-control media. New downhole data are required for better understanding and prevention of production impairment. We introduce real-time completion monitoring (RTCM), a new nonintrusive surveillance method that uses acoustic signals sent via the fluid column to identify permeability impairment in sand-screened completions. The signals are carried by tube waves that move borehole fluid back and forth radially across the completion layers. Such tube waves are capable of instant testing of the presence or absence of fluid communication across the completion and are sensitive to changes occurring in sand screens, gravel sand, perforations, and possibly in the reservoir. The part of the completion that has different impairment from its neighbors will carry tube waves with modified signatures (velocity, attenuation) and will produce a reflection from the boundary where impairment changes. We conduct a laboratory experiment with a model of a completed horizontal borehole and focus on effects of sand-screen permeability on transmitted and reflected acoustic signatures. These new findings form the basis of an RTCM method that can be thought of as "miniaturized" 4D seismic and as a "permanent log" in an individual wellbore. We present experiments with a fiber-optic acoustic system that suggest a nonintrusive way to install downhole sensors on the pipe in realistic completions and thus implement real-time surveillance with RTCM.

## INTRODUCTION

Completions lie at the heart of deepwater production and constitute a large portion of overall well cost. Great multidisciplinary effort is expended up front to design the completions correctly. This contrasts greatly with the production stage, in which little information is available to detect problems, optimize inflow, and prevent expensive workovers. Sand-screen plugging, incomplete packing, development of "hot spots" in screens, destabilization of the annular pack, fines migration, near-wellbore damage, crossflow, differential depletion, compartmentalization, and compaction represent a typical list of challenges that are extremely difficult to decipher based on only several permanent pressure and temperature gauges (Wong et al., 2003).

Many problems can be identified by production logging, but that is costly and not in real time. Permanent pressure and temperature sensors placed across the sand face can provide critical information to diagnose the completion problems, and the service industry is developing tools to make such sensing feasible in the future. However, these new pressure and temperature data are unlikely to lead to unambiguous identification of the problems above because of the multitude of parameters characterizing complex completions and reservoirs that remain unconstrained by our data.

For example, let us take the issue of underperforming deepwater wells. Well performance encompasses large-scale reservoir issues, such as compartmentalization, as well as changes in local well skin over time caused by completion, perforations, and near-wellbore effects. Therefore, multiple explanations can be given to the problem. Apparent compartmentalization and ubiquitous U-shaped boundaries can be one answer on a reservoir scale. Yet those boundaries rarely are confirmed by 4D seismic or other data. Shale draping is an alternative reservoir-scale scenario that can lead to well underperformance.

Another wellbore-scale explanation suggests that well productivity declines with time because of the loss of the so-called $kh$ product, where $k$ and $h$ are reservoir permeability and thickness, correspondingly. The differential depletion model (P. Fair and F. Rambow, personal communication, 2003) argues that this loss occurs mainly because of reduction in producing thickness, although the exact mechanisms of flow impairment still are debated. Similarly, reduction in permeability is another alternative explanation offered by Pourciau et al. (2003), although the amount of this reduction (85% to 90%) is not consistent with laboratory measurements.

Existing sparse data from wells can support any of these scenarios, thereby confirming that the problem is underconstrained. Therefore, to distinguish between these quite different scenarios, we need more downhole data at various scales that can characterize various components of the production system unambiguously.

In the context of deepwater completions, there is an additional emphasis on sand control because it is believed that "managing produced sand, as we understand it, is generally a costly and mostly unworkable solution for the Gulf of Mexico but can work well in other places where there is some grain-to-grain cementation present," according to Scott Lester of Shell (Sand Control, 2005, p. 4). The presence of sand-control media between the reservoir and the wellbore introduces additional cost and complexity and requires proper management. The goal is a solution that "is installed correctly the first time and is tough enough to control sand production for the life of the reservoir, [thus] avoiding impairment and the need for any intervention," Lester said (Sand Control, 2005, p. 4).

However, to achieve this goal in an environment with the ever-increasing complexity and escalating costs likely would require sand-screened completions permanently equipped with proper surveillance tools that deliver real-time information about performance of the various components of the production system. First of all, this should allow dissection of the current issues: "To come up with a (sand-control) system that is less prone to problems, the root cause of existing problems must first be understood," Lester said (Sand Control, 2005, p. 7).

Once issues are fully understood, then smart, on-demand intervention or remediation may become possible. The high cost of deepwater well "jewelry" (sand screens and other equipment) and intervention can justify the presence of smart surveillance tools that would not be economical in any other environment. This understanding is shared throughout the industry. "For example, sand control may be part of a completion in deep water when it would not be included in a similar completion on land or on the continental shelf," said Rick Dickerson of Chevron (Sand Control, 2005, p. 6). Dickerson added that among the key criteria of well performance, reliability, and cost, performance and reliability will usually trump cost. "The sand-control method needs to last the life of the reserve," Dickerson said (Sand Control, 2005, p. 6).

This paper describes real-time completion monitoring (RTCM) — a new method that uses acoustic waves to assess changes in permeability occurring in the sand screen, gravel pack, and individual perforations. It is complementary to other in-well monitoring methods such as the real-time casing imager (Rambow et al., 2005;

Childers et al., 2007), which allows us to monitor structural integrity (static deformations) of sand screens and thus provides an understanding of compaction and other strain-related conditions.

In essence, the acoustic monitoring method is like a permanently installed stethoscope and sonograph at the chest of the patient (sand face of the reservoir). The sonograph constantly conducts an active health check of the well, whereas the stethoscope passively listens to sneezing and coughing within the reservoir. Early detection and proper diagnostics follow as a natural outcome of permanent monitoring so that proper treatment (workover) can be delivered before issues get out of hand. Permanent monitoring also can serve as additional insurance to safeguard expensive completion and sand-control jewelry as well as the borehole itself. In addition, RTCM can deliver a stream of new data to help in understanding other sand-screen and completion issues and eventually to contribute to proper resolution of the well underperformance problem.

This paper is organized as follows. First we briefly review borehole wave propagation in open and cased boreholes. Then we introduce a flow-loop setup with a section of a horizontal well used for laboratory experimentation. In this study, we focus on experiments with plugged and open sand screens in the absence of gravel pack. To develop an understanding, we introduce and analyze simple two- and four-layer cylindrical models using analytical and numerical methods. Sand screens are modeled as poroelastic Biot layers. Then we present measured transmission and reflection signatures and compare them with those predicted by modeling.

We conclude that acoustic signatures of open and plugged screens are distinguished in the experiment. We also confirm that the poroelastic description is appropriate and obtain semiquantitative agreement between data and models.

In the next section, we present numerical modeling of a gravel-packed completion with sand, which is the subject of future experimentation. The last section describes tests of a fiber-optic system for acoustic measurements and suggests downhole instrumentation for actual wells.

## ACOUSTIC WAVES IN BOREHOLES

To apply the acoustic method, we need to understand wave propagation in a realistic downhole environment. Prior to examining cased boreholes with completions, it is instructive to review existing knowledge on the effect of permeability on acoustic signatures in open and cased boreholes.

### Open boreholes

Figure 1 depicts a model of an open borehole in a porous permeable formation filled with fluid — an environment typical for wireline acoustic logging. Such a model has been investigated by various authors (Rosenbaum, 1974; Schmitt et al., 1988; Chang et al., 1988; Tang et al., 1991; Liu and Johnson, 1997; Endo, 2006). The tube, or Stoneley, wave is a fundamental axisymmetric mode that exists from zero frequency (White, 1983). At low frequencies, it represents a pistonlike motion of the fluid column and dominates wave propagation.

When formation shear velocity is larger than fluid velocity (fast formation), the tube wave becomes completely trapped — a mode that does not attenuate in impermeable formations. When the tube wave encounters a permeable region, it starts to slow down and attenuate because fluid communication occurs between the formation
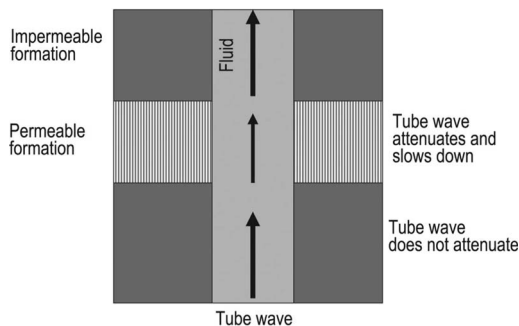


Figure 1. Depiction of a borehole in a formation with varying permeability. The tube wave attenuates and slows down when it encounters the permeable interval that can exchange fluids between borehole and formation.

and the wellbore. This communication leads to an energy loss in the form of leaking slow Biot waves inside the formation.

Modeling predicts that at low frequencies, tube-wave velocity decreases and attenuation increases with increasing fluid mobility (permeability/viscosity). These predictions were validated in the laboratory (Winkler et al., 1989) and became a foundation for the only "direct" and continuous technique of estimating in situ permeability from wireline logs (Chang et al., 1988; Tang et al., 1991; Liu and Johnson, 1997; Endo, 2006).

The presence of mud cake restricts fluid communication and makes tube-wave signatures less sensitive to formation permeability (Liu and Johnson, 1997; Tichelaar et al., 1999). In the limiting case of a hard mud cake, fluid pressures in the borehole and the formation become completely unrelated — tube waves experience no attenuation or slowdown and propagate exactly the same as if the well were surrounded by an impermeable formation (Liu and Johnson, 1997).

Boundaries between formations with different permeabilities also cause reflected tube waves (Tang and Cheng, 1993). Figure 2 illustrates the effect of permeability using a simple model of a 2.4-m-thick reservoir embedded between two impermeable half-spaces (Bakulin et al., 2005). The bottom black curve shows the response of an impermeable elastic formation. Some reflection exists as a result of mismatch of tube-wave velocities between layer and half-spaces caused by the contrast in velocities and densities.

An increase in layer permeability leads to a dramatic increase in tube-wave reflectivity, especially at low frequencies. This added reflectivity results from increased fluid communication; a more permeable formation leads to a larger slowdown in tube-wave velocity inside the layer and therefore results in a larger contrast in properties that control the reflection.

All computed responses assume complete communication between formation and borehole fluid described by the so-called open-flow boundary conditions (Deresiewicz and Skalak, 1963). If fluid communication is terminated (e.g., hard mud cake), then all the responses collapse down to the black curve, which corresponds to the impermeable elastic case. This highlights the fact that tube-wave signatures are affected only when fluid communication is present. For partial fluid communication, responses would be between elastic impermeable and corresponding open-flow poroelastic solutions.
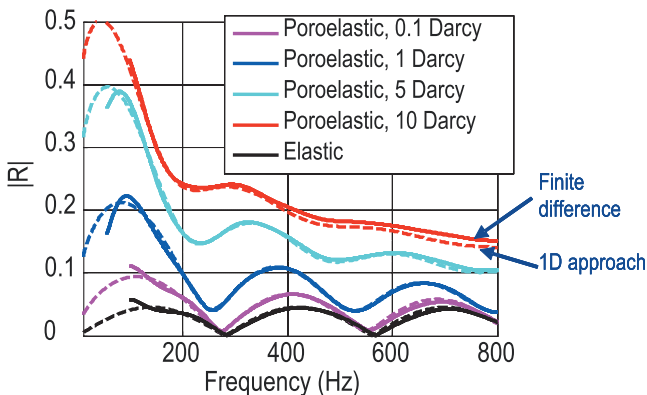


Figure 2. Amplitude of the tube-wave reflection coefficient as a function of frequency for a model of a single poroelastic reservoir layer between two half-spaces of caprock. Dashed lines are derived with a 1D effective wavenumber approach, and solid lines are computed with a finite-difference code. The bottom curve represents reflection from an elastic (impermeable) zone between two elastic half-spaces (after Bakulin et al., 2005).

We conclude that tube waves are capable of "instant" testing for the presence or absence of fluid communication across the borehole wall inside a particular layer. If the fluid communication is absent as a result of mud cake or lack of formation permeability, then no slowdown or attenuation is observed. If fluid communication is present, then slowdown and attenuation are observed. Similarly, in a reflection configuration, increased fluid communication leads to a larger reflection.

In the next sections, we generalize these simple principles to cased, completed boreholes with sand-screened completions.

## Cased and completed boreholes

A cased and completed well has additional layers between the formation and borehole fluid. In a simplified model of a sand-screened cased completion, we observe the following cylindrical layers (from inside out): borehole fluid, sand screen, gravel sand, casing, and formation (Figure 3). Perforations act as communication channels that connect the borehole with the formation through casing. In open-hole completions, the casing and perforations are absent, and formation fluid communicates directly with the borehole through the gravel pack and sand screen. The sand screen and gravel pack prevent migration of reservoir sand into the wellbore and maintain the structure of the reservoir around the wellbore.

This more complex model of a completed well has one essential similarity to the simple open-hole model; in a normal scenario of a flowing well, there has to be fluid communication across all layers of the completion. Lack of fluid communication in any intermediate layer (screen or perforations) will disconnect the flow of reservoir fluid into the borehole. The aim of the current study is to analyze the effect of broken fluid communication across the sand screen or perforations through the signatures of tube waves.

Despite high-level similarity, key acoustic distinctions between the models of open-hole and sand-screened completions exist:

- The completion has additional solid layers of sand screen and casing (both made of steel).
- Only a single poroelastic layer and a single interface are present in the open-hole model, whereas in the sand-screened completion, we have multiple poroelastic layers (perforated casing, formation, gravel sand, sand screen) and multiple poroelastic interfaces between them.
- Gravel sand and sand screen are very different from reservoir
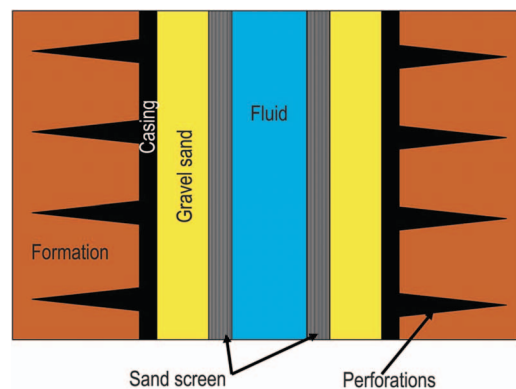


Figure 3. Schematic cross section of a sand-screened completion in a cased hole.

rocks; they possess extremely large permeability ($>100$ D). In addition, gravel sand has very low shear velocity ($<100$ m/s).

The effects of casing and (impermeable) sand screen can be understood partially from studies of wave propagation in a producing well with tubing and casing (Ziatdinov et al., 2005) or in open holes with drillpipe (Rama Rao and Vandiver, 1999). In both cases, the inner pipe and the annulus are filled with the same or a different fluid. The key distinction between these analogue models and the sand-screen completion is the following:

- Tubing, drillpipe, and casing are completely impermeable, whereas sand screen, gravel sand, and casing are highly permeable and, in the normal case, are open to flow.
- The annulus is filled with fluid that has no shear rigidity, whereas the gravel sand in the sand-screened completion is likely to have some small shear rigidity.

Finally, we should mention two techniques that already use tube waves for monitoring hydraulic fracturing in producing cased and perforated wellbores. The first technique is the so-called tube-wave reflection logs (Medlin and Schmitt, 1994). This technique analyzes the strength of tube-wave reflections along the perforated interval that was hydraulically fractured. To conduct tube-wave reflection logging at frequencies of ~300 to 3000 Hz before and after stimulation allows one to assess the quality of hydraulic fracturing along the perforated interval.

The second technique, "hydraulic impedance testing" (Holzhausen and Gooch 1985; Paige et al., 1995), consists of periodically
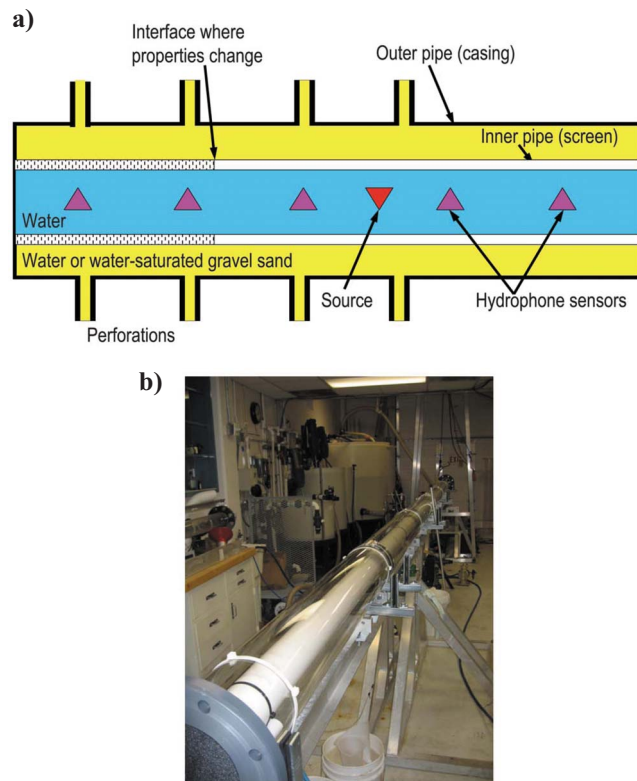


Figure 4. (a) Sketch of the flow-loop setup with the model of sand-screened completion in horizontal well. (b) Photograph of the actual setup with a glass outer pipe (no perforations).

pulsing the stimulation well with very low-frequency tube waves ($<10$ Hz) and looking for changes in various signatures of reflected signals to estimate the time of opening and the parameters of a hydraulic fracture behind a perforated casing.

In the first technique, a source and a receiver are placed in the wellbore next to the fracture, and therefore, high-frequency reflections can resolve the flow properties of individual vertical intervals of a few meters. In the second technique, the signal is sent and received from the wellhead, and then only very low frequencies can be recorded. As a consequence, this technique has poor vertical resolution, and only averaged properties of the whole fracture can be evaluated. Nevertheless, both techniques illustrate the successful use of tube waves to sense the increase in fluid communication between wellbore and formation caused by the opening of a hydraulic fracture.

RTCM is a combination of a permanent log (transmission) and mini-4D seismic in a well (reflection), which combines elements of all of the above-mentioned techniques. The key distinction is that RTCM is applied to a special completion environment composed of man-made (screen, casing, gravel sand) and natural (formation) components, the permeability of which needs to be monitored over time. In this proof-of-concept study, we focus on a laboratory experiment that simulates a realistic completion and compares the results with analytical and numerical modeling.

## LABORATORY SETUP WITH A HORIZONTAL WELL MODEL

Figure 4 depicts the schematics and photograph of a horizontal flow-loop setup used for the experimental measurements. The outer pipe (casing) of ~30 ft (9 m) consists of six 5-ft sections joined together and attached to the underlying support rail. The inner pipe (sand screen) is positioned inside using plastic centralizers.

The annulus between the inner and the outer pipe can be filled with water or water-saturated gravel sand. Measurements are conducted with a hydrophone array and a piezoelectric source lying at the bottom of the inner pipe. The source excites a broadband impulsive waveform with a controlled dominant frequency. Twenty-four hydrophone sensors with 35-cm spacing record the resulting wavefield. To reduce background (building/air conditioning) noise, stacking of multiple records is used.

RTCM is intended to distinguish among four completion scenarios (Table 1) using tube-wave signatures. *Open* and *Closed* denote two extreme cases of presence or absence of full fluid communication. "Partial" fluid communication should manifest itself with intermediate signatures between these two bounds. Signatures examined include propagation velocity and attenuation of tube waves as well as transmission and reflection amplitudes from interfaces where contacting media are described by different scenarios.

**Table 1. Completion scenarios.**

|            | Flow conditions at sand screen | Flow conditions at perforations |
|------------|:------------------------------:|:-------------------------------:|
| Scenario 1 | Open   | Closed |
| Scenario 2 | Closed | Closed |
| Scenario 3 | Open   | Open   |
| Scenario 4 | Closed | Open   |

In this study, we present experimental measurements for scenarios 1 and 2 in the absence of gravel sand and compare them with modeling. In the last section, we present numerical modeling of gravel-packed completions for the first two scenarios. Experiments with sand as well as the remaining two scenarios will be described elsewhere.

## WAVE PROPAGATION IN A SIMPLIFIED COMPLETION MODEL AS IN LABORATORY SETUP (NO GRAVEL PACK)

Here we present a simple model that describes wave propagation in the laboratory setup. This model will need only a minor modification to be applicable to the real in situ environment. Actual sand screens can be quite complicated (Figure 5), but we start with the assumption that a screen is represented by a homogeneous effective pipe, both in terms of mechanical and hydraulic properties. If this pipe is not permeable (plugged screen), then the laboratory setup can be simplified to this four-layer model: fluid — elastic inner pipe (screen) — fluid — elastic outer pipe (casing).

This model of two concentric elastic pipes with a free outer boundary (air) supports four axisymmetric wave modes at low frequencies:

- TI: tube wave supported by the inner pipe
- TO: tube wave supported by the outer pipe
- PI: plate- or casing-type wave related to the inner pipe
- PO: plate-type wave related to the outer pipe

Appendix A describes the nature of the modes and explains how velocity of these modes depends on completion parameters.

Figure 6a-c shows synthetic seismograms for such a four-layer model with parameters from Tables 2 and 3. Seismograms are computed with a finite-difference code developed jointly by Keldysh Institute of Applied Mathematics (Russia) and Shell. The dominant arrival is a fast tube wave associated with the outer pipe (TO), whereas the slow tube wave supported by the inner pipe (TI) is weaker. Plate waves can be seen only with substantial amplification. Plate-wave velocities are almost independent of frequency. The fast tube wave is slightly dispersive, whereas the slow tube wave experiences moderate dispersion (Figure 6d).

If formation is added outside the casing, then the outer plate wave (PO) disappears. If the annulus between the casing and the screen is filled with sand, then there are only one tube wave and one plate wave associated with the composite structure of the completion (see "Completion with a gravel pack"). Therefore, the presence of two

tube waves is a diagnostic for a completion without a gravel pack (or fluidized gravel pack).

If the inner pipe becomes permeable (open to flow sand screen), then the same number of wave modes remains, but their velocities and attenuation become altered. Simply speaking, both tube waves experience attenuation and slowdown.

In the next section, we present experimental data and compare them with a finite-difference poroelastic modeling. Here we explain only the choice of parameters for the sand screens. Sand screens open to flow are modeled as a homogeneous pipe made of effective poroelastic Biot material (Biot, 1956). To resort to effective medium theory may not be fully justified because microelements, such as perforations in a base pipe or slots, are of the same dimensions as the pipe thickness. Nevertheless, data suggest that tube waves with wavelengths of several meters "see" the screen as an effective pipe and justify a simple model to understand the effect of permeability changes on tube-wave signatures.

Our initial guess for the poroelastic parameters of polyvinyl chloride (PVC) and aluminum screens is summarized in Table 2. The radial permeability of the screens is estimated using a simple analytical model with an array of parallel slits or fractures.

In cases when perforations are closed (scenarios 1 and 2), the outer layer is considered as an impermeable pipe with a traction-free outer boundary. Complete plugging (scenario 2) is modeled as a no-
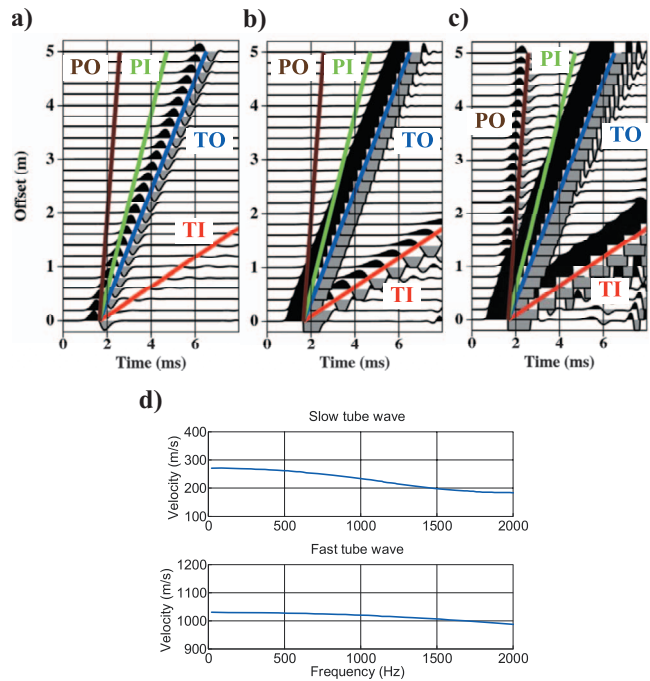


Figure 6. Pressure seismograms with (a)-(c) successive amplifications and (d) dispersion curves for a four-layer model with closed pores (no gravel pack) from monopole source. Parameters and geometry are given in Table 2 and Table 3 (version 2 of glass setup with PVC 13%). The hydrophone array is at the center of the pipe, and the source central frequency is 1000 Hz. (a) The largest arrival is a fast tube wave (TO: 1030 m/s) related to the outer glass pipe. (b) The smaller arrival is a slow tube wave (TI: 270 m/s) related to the plastic inner pipe. (c) Plate waves are of even smaller amplitude (brown, PO: 5410 m/s; green, PI: 1630 m/s). (d) Theoretical dispersion curves for the fast and slow tube waves.
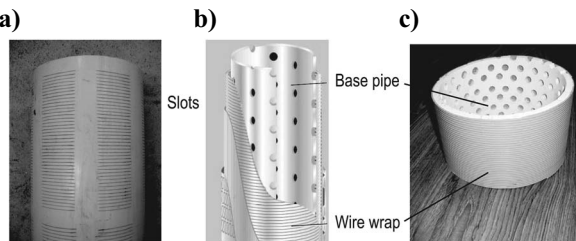


Figure 5. Sand screens: (a) slotted PVC screen (4% porosity) used in the current experiments; (b) premium screen, named as Excluder; (c) wire-wrapped PVC screen (13% porosity). Image (b) is from Baker Web site.

flow boundary condition between the screen and the surrounding fluids (Deresiewicz and Skalak, 1963).

## COMPLETION WITHOUT GRAVEL PACK: EXPERIMENT VERSUS MODELING

Experiments were conducted with a glass outer pipe and a PVC inner pipe (Figure 4). The geometry of the setup is captured in Table 3. To model an open sand screen (open pores), we use a PVC pipe with 0.0002-m (0.008-in) slots (Figure 5a). The plugged sand screen was modeled with a blank PVC pipe without slots and is referred to as "closed pores." The aluminum setup is used in the last section for modeling future experiments with the sand.

### Transmission signatures

Let us first analyze transmission signatures — velocity and attenuation — in the presence of open and plugged screens. Figure 7 compares wavefields recorded in the case of no screen and in the case of a screen with open and closed pores. In the absence of a screen, there is only one (fast) tube wave present with velocity of about 1050 m/s. It experiences some amplitude loss, possibly related to intrinsic attenuation in the glass as well as in the thick recording cable.

When an impermeable inner pipe is added (closed pores), an additional slow tube wave appears, whereas the fast wave starts to be slightly more attenuative as a result of high absorption in PVC. When the inner pipe becomes slotted, fluid on both sides of the PVC screen starts to communicate, and this leads to a very strong attenuation of both tube waves. Median filtering can separate the fast wave (Figure 8) and slow wave (Figure 9) and reveal the presence of multiple reflections of each wave at the joints between the 5-ft pipe segments. Figure 10 shows more clearly that the slow wave is absent without a screen, is present in a screen with closed pores, and becomes more attenuative and low frequency in open pores. Thus, a greatly increased attenuation of both fast and slow tube waves is the first-order diagnostic for open screens (open pores), whereas reduced attenuation is characteristic for plugged screens (closed pores).

**Table 2. Material parameters used in modeling.**

| Parameters | Gravel sand | PVC slotted screen (4%) | PVC wire-wrapped screen (13%) | Aluminum wire-wrapped screen | Fluid-filling in porous layer | Glass | Aluminum |
|---|---|---|---|---|---|---|---|
| Bulk modulus $K$ (GPa) | | | | | 2.25 | 35.6 | 66.4 |
| Shear modulus $\mu$ (GPa) | | | | | | 26.7 | 25.6 |
| Density $\rho$ (kg/m³) | 2052 | 1384 | 1348 | 2480 | 1000 | 2230 | 2700 |
| Grain bulk modulus $K_g$ (GPa) | 37 | 4.049 | 4.049 | 66.4 | | | |
| Grain shear modulus $\mu_g$ (GPa) | 44 | 1.248 | 1.248 | 25.6 | | | |
| Grain density $\rho_g$ (kg/m³) | 2670 | 1400 | 1400 | 2700 | | | |
| Dry bulk modulus $K_0$ (GPa) | 1.35 | 3.482 | 2.956 | 50.9 | | | |
| Shear modulus $\mu$ (GPa) | 0.01 | 1.211 | 1.154 | 19.4 | | | |
| Porosity | 0.37 | 0.04 | 0.13 | 0.13 | | | |
| Permeability (D) | 100 | 130 | 50 | 50 | | | |
| Viscosity (Pa s) | | | | | 0.001 | | |
| Tortuosity | 1.5 | 1.5 | 1.5 | 1.5 | | | |
| $P$-wave velocity [saturated, $f = 0$ Hz] (m/s) | 1780 | 2004 | 1980 | 5600 | 1500 | 5647 | 6100 |
| $S$-wave velocity [saturated, $f = 0$ Hz] (m/s) | 70 | 935 | 925 | 2800 | | 3458 | 3077 |

**Table 3. Geometry and material composition of the setup.**

| | Glass setup (current experiments) | | | Aluminum setup (modeling and future experiments) | |
|---|---|---|---|---|---|
| | | Version 1 (4-in) | Version 2 (5-in) | | |
| Cylindrical layers | Material | Outer radius (m) | Outer radius (m) | Material | Outer radius (m) |
| Layer 1 | Water | 0.0508 | 0.0635 | Water | 0.0635 |
| Layer 2 | PVC | 0.0572 | 0.0700 | Aluminum | 0.0667 |
| Layer 3 | Water | 0.1006 | 0.1006 | Sand | 0.1032 |
| Layer 4 | Pyrex glass | 0.1076 | 0.1076 | Aluminum | 0.1095 |

Additional diagnostics can be established by analyzing energy distribution as a function of frequency between these two cases. Because the experimental data are complicated by the presence of additional reflections at the pipe joints, this analysis is performed best by using the slowness-frequency spectra shown in Figure 10.

Figure 11 represents the averaged velocity spectrum over the entire frequency range, or the horizontal stack, of Figure 10. Both fast and slow tube waves with approximately the same velocities of 350 m/s and 1100 m/s are present in the plugged and open cases (Figure 11); however, the slow wave is completely absent without a screen. In a plugged screen, the fast wave carries maximum energy in the frequency range of 300 to 600 Hz, which is close to the dominant frequency of the source, whereas lower and higher frequencies carry less energy (Figure 10).

In contrast, the spectrum of the fast wave in an open screen has a big energy "hole" between 300 and 600 Hz, where the fast wave is attenuated so strongly that even higher frequencies (600 to 900 Hz) carry more energy. This behavior is summarized in Figure 12, which confirms that fast-wave energy is severely attenuated in the medium-frequency range, whereas it still is preserved in the high-frequency range. As for the slow tube wave, it exists mainly at frequencies below 600 Hz and also is attenuated. Surprisingly, its amplitude "lightens up" at low frequencies for open pores where it is larger than the amplitude of the fast wave (Figures 11 and 12).

Let us compare this behavior with the numerical modeling. Figure 13 shows theoretical dispersion curves for the case of closed pores. The fast tube wave experiences little dispersion below 2000 Hz and
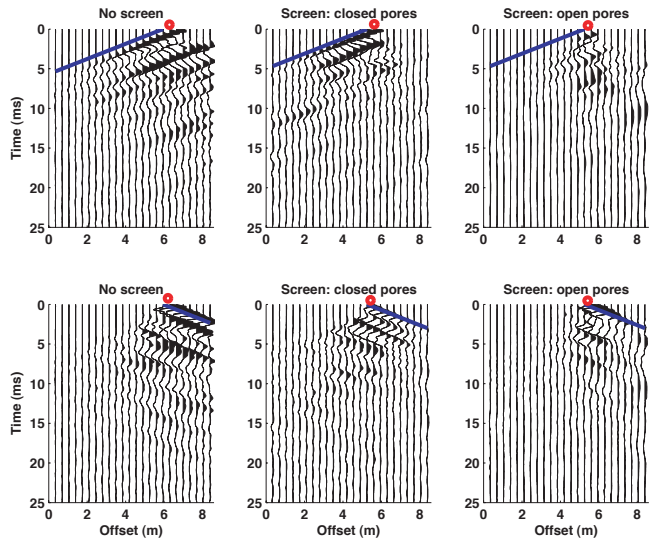
Figure 8. Same as Figure 7 but after median filtering with the velocity of the fast tube wave 1050 m/s (dark blue line). The top row shows leftgoing energy, and the bottom row shows rightgoing energy. The direct arrival from the source, as well as multiple reflections from regularly spaced pipe joints, is visible. A screen with closed pores leads to small attenuation, whereas an open screen leads to a very strong attenuation of the fast wave. Displays for each case are normalized separately by the maximum amplitude.
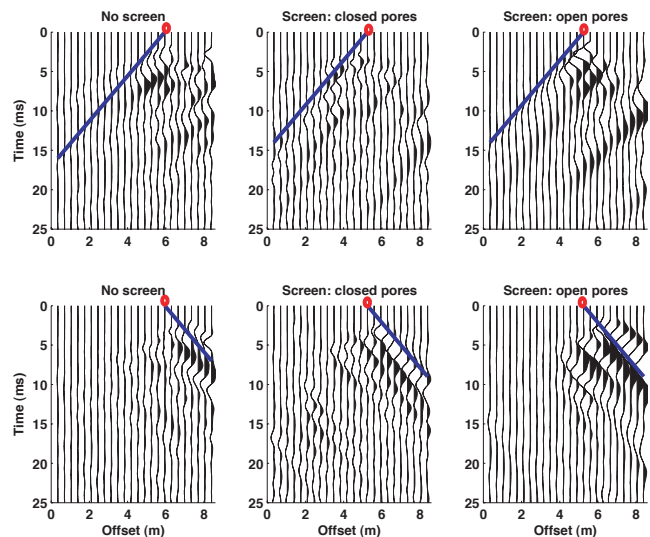
Figure 9. Same as Figure 7 but after median filtering with the velocity of the slow tube wave 350 m/s (dark blue line) and bandpass filtering (50 to 500 Hz). In the absence of a screen, the slow wave is not traceable (some incoherent remainder of the fast wave is visible). In a screen with closed pores, the slow wave is most prominent and traceable for the longest distance, whereas in an open screen, it experiences strong attenuation. Note that the amplitudes of all displays are increased by a factor of three compared to that in Figure 7.
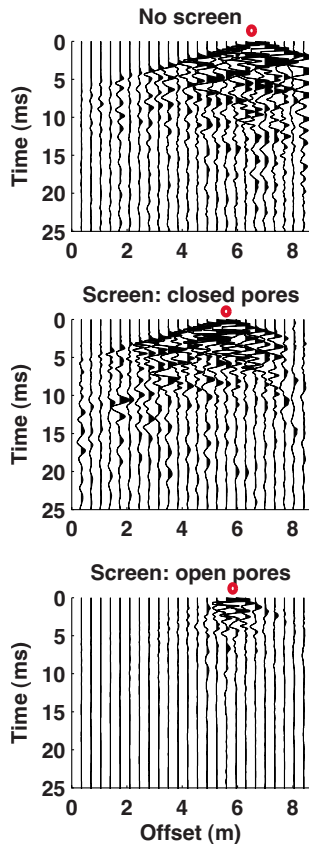
Figure 7. Seismograms recorded in the glass setup by hydrophone array from a piezoelectric source (red symbol) with a dominant frequency of 500 Hz. The label *No screen* shows traces in the absence of an inner pipe, *open pores* is for a slotted sand screen (version 2 from Table 3), and *closed pores* is for a blank pipe without slots (version 1 from Table 3). Note that the fast tube wave is attenuated least in the absence of a screen, somewhat attenuated in closed pores, and substantially absorbed in open pores. The two lower displays correspond to slightly different dimensions of the inner pipe (version 1 and 2) and to slightly different locations of the source. The source and receiver array is lying at the bottom of the inner pipe.

matches experimentally observed values. An increase in diameter of the impermeable inner pipe should result in a slowdown of the second-tube wave velocity from 350 to 280 m/s (Figure 13). Although for closed pores (4-in inner pipe) the slow velocity is well matched, for open pores (5-in inner pipe), the velocity is higher than predicted. Most likely, this is the result of variation in elastic properties of PVC used for manufacturing blank 4-in pipe and slotted 5-in screen.

Figure 14 shows synthetic seismograms computed for a glass set-up with our best guess of the poroelastic parameters shown in Table 2. Similar to the experiment, in the case of closed pores, we observe two tube waves, with the fast tube wave dominating in amplitude. In the presence of a screen with open slots, both waves experience strong changes. The fast tube wave experiences moderate attenuation and change of waveform (Figure 14a). The slow tube wave transforms into a complex packet with weak amplitude, rather slow velocities, and a very strange character (Figure 14c). If we connect the points where the phase is changing inside the packet, we arrive at

approximately the velocity of the propagating slow Biot wave in the porous screen material (~80 m/s). Because the central frequency of the source (500 Hz) is much higher than the critical Biot frequency (30 Hz), interference with the slow Biot wave in the porous screen might be a reason for a complicated wave packet.

Figure 11. Velocity spectra averaged over all frequencies from Figure 10 for cases of no screen (top), screen with open pores (middle), and screen with closed pores (bottom). The maximum at ~350 m/s corresponds to the slow tube wave, whereas the peak at 1100 m/s corresponds to the fast tube wave. Note that a slow tube wave is absent when there is the sand screen.
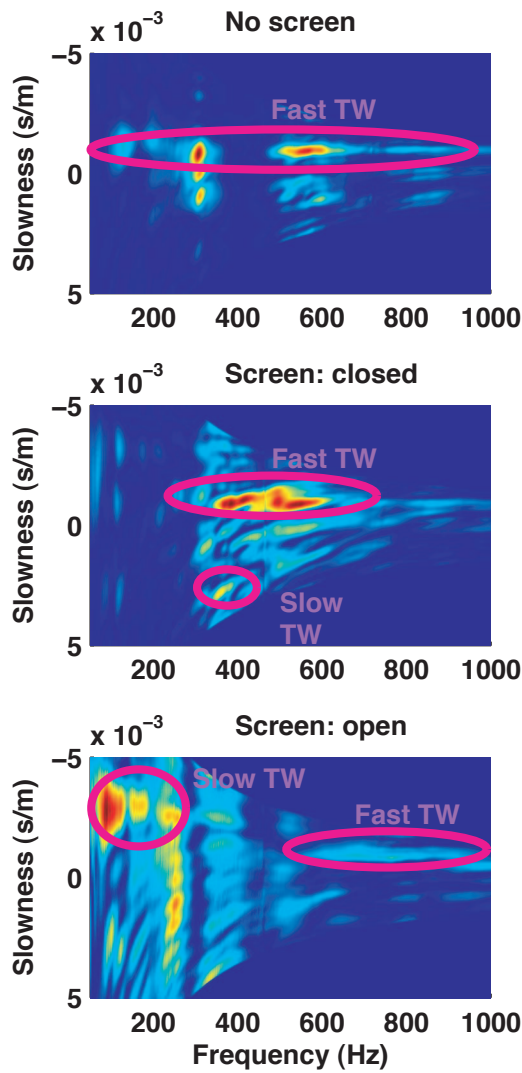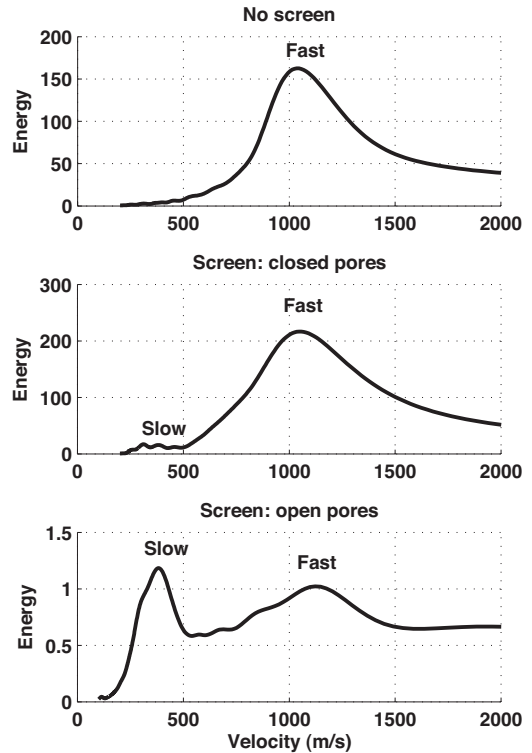
Figure 10. Slowness-frequency display of experimental data in the absence of a screen (top), with a closed screen (middle), and with an open screen (bottom). Input traces are taken from Figure 7 (traces to the left of the source are used). Red hues denote high energy, whereas blue hues show low energy. Note that the energy scale is normalized separately for each display.
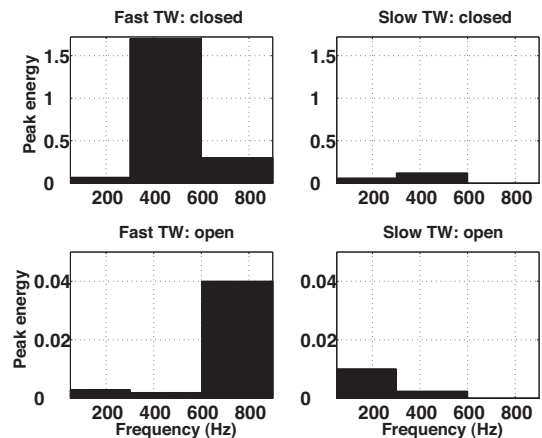
Figure 12. Distribution of energy between the fast tube wave (left) and the slow tube wave (right) for experimental data with closed and open screens shown in Figure 7. To obtain robust estimates in the presence of noise, we stack the energy within low-frequency (50- to 300-Hz), medium-frequency (300- to 600-Hz), and high-frequency (600- to 900-Hz) bands. Note the very strong attenuation of the fast tube wave in the medium-frequency range.
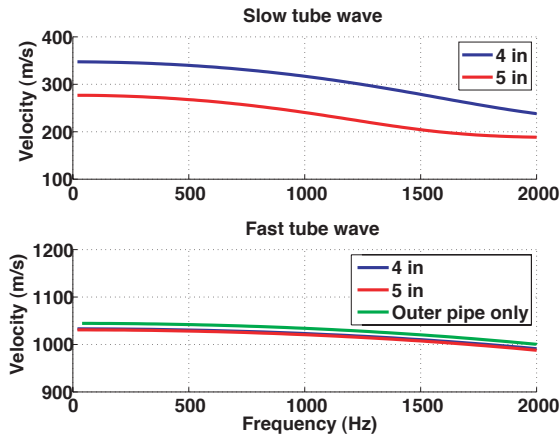
Figure 13. Tube-wave dispersion curves for two geometries of the glass setup from Table 3: *4 in* denotes version 1, and *5 in* denotes version 2. The inner pipe is considered to be an impermeable elastic material with velocities and densities as for the slotted PVC with 4% porosity from Table 2. The green curve shows dispersion in the absence of the inner pipe when only the fast wave is present.
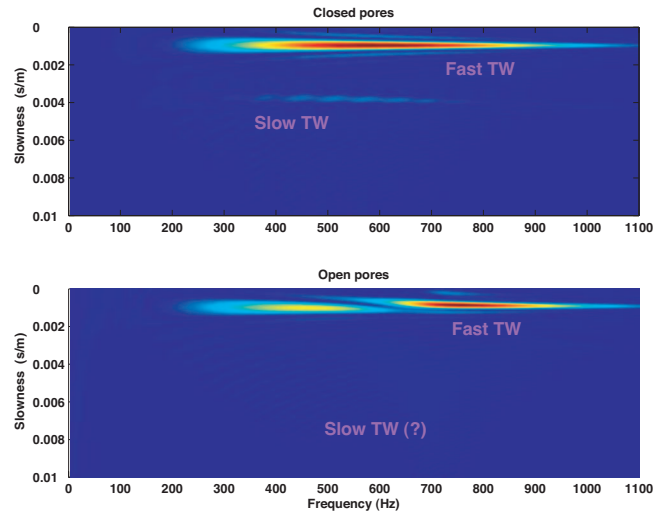
Figure 15. Slowness-frequency spectrum for the synthetic seismograms from Figure 14. The fast tube wave dominates the spectrum. For closed pores, the slow tube wave has a broadening peak toward lower frequencies, indicating dispersion. In the presence of open slots, the fast wave experiences strong attenuation that is particularly anomalous in the medium-frequency range (350 to 700 Hz).
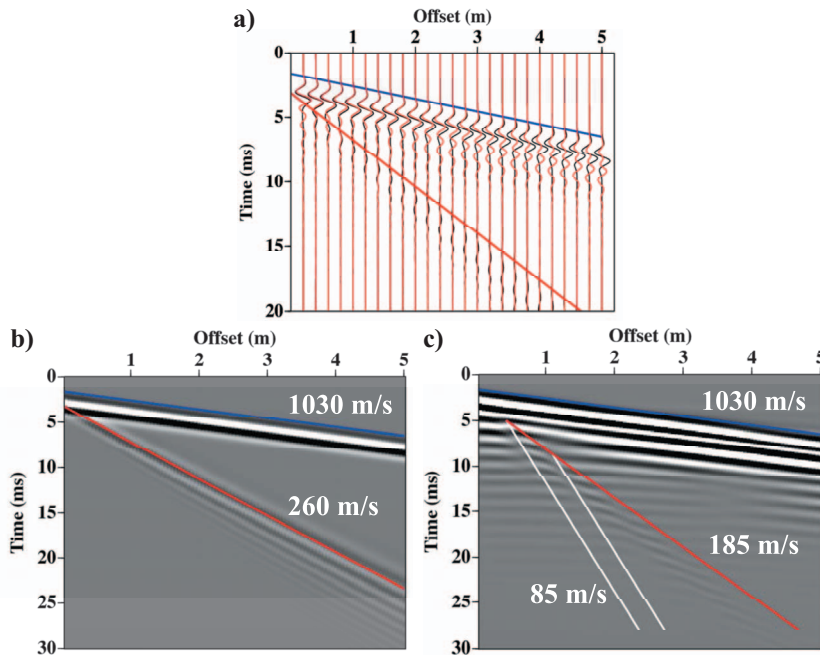


Figure 14. Synthetic pressure seismograms computed for open and closed pores in the glass setup by the poroelastic reflectivity method (version 2 of Table 3). The central frequency of the source is 500 Hz. (a) Overlay of seismograms for open (red) and closed (black) pores shows that the fast tube wave in a permeable screen experiences strong attenuation and dispersion and a change of waveform. Model parameters are taken from Table 2 (4% PVC). Blue and red lines denote moveout velocities of the fast (1030 m/s) and slow (280 m/s) tube waves. (b) Shadow display for closed pores highlights the strongly dispersive slow tube wave. (c) Shadow display for open pores with a higher magnification shows that in open pores, the slow tube waves transform into a complicated packet of energy with very low velocities and a staircase pattern. White lines connecting the breaks in the phase have slopes close to slow *P*-wave velocity in the porous screen material.

The following physical interpretation can be given to the modeled results. A tube wave is born when the pistonlike motion of the fluid inside the pipe creates a radial expansion that is resisted by the elastic pipe. The slow wave is supported mainly by the inner pipe (Appendix A). When this pipe becomes slotted, radial movement of the fluid no longer is resisted because liquid can freely escape to the annulus, thus leading to a strong attenuation of this wave.

In contrast, the fast wave is supported mainly by the outer glass solid pipe. When the inner pipe becomes permeable, pistonlike motion of the fluid in the fast wave also can exchange the fluid between the outer and inner fluid columns, thus creating a moderate attenuation.

Slowness-frequency spectra for open pores (Figure 15) shows that similar to the experimental results, the fast wave experiences anomalously high attenuation in the medium-frequency range of 350 to 700 Hz. In addition, velocity slows down at low frequencies and the energy peak becomes broader, thus indicating dispersion. Figure 16 verifies that the fast tube wave in an open screen is slowed down at low frequencies but experiences slight speedup at high frequencies. Comparison of Figures 16 and 12 confirms the qualitative agreement between experiment and modeling. In both cases, the fast wave exhibits anomalous amplitude decrease in the medium-frequency range but still preserves higher and lower frequencies. This amplitude decrease cannot be explained by the spectra of the source

wavelet and therefore should be attributed to anomalous attenuation caused by fluid movement through the slotted porous screen.

The frequency range with resonance attenuation is controlled by permeability. For instance, when permeability decreases from 130 to 50 D (13% PVC from Table 2), this band moves from 350–700 Hz to 600–1000 Hz (i.e., the lower the permeability, the higher the frequency of the band with anomalous attenuation of the fast wave). This is also consistent with experimental data because the plugged screen (0 Darcy) does not exhibit any anomalous attenuation; in this case, this band will be at a very high or infinite frequency. Therefore, central frequency of the band with anomalous attenuation of the fast tube wave is an additional robust diagnostic of the screen

permeability. We should note that in both cases, central frequency of the source is much higher than the critical Biot frequency for the screen.

To obtain more quantitative agreement with the data, we need to improve our estimates of poroelastic parameters. Future studies also should consider the effects of strong anisotropy in the hydraulic and acoustic properties of the slotted screen (Figure 5a) that is approximated by an isotropic poroelastic material.

As for the slow tube wave, it remains unexplained why open-pore modeling predicts rather strong dissipation, strange character, and strong slowdown (Figure 14c), whereas experiment shows that the slow wave is simpler and of comparable amplitude to the fast wave at low frequencies (Figure 12).

## Reflection signatures

The difference in velocity and attenuation between completions with open and plugged screens also leads to reflections at the boundaries where properties change. We now examine transmission-reflection at the single interface between open and plugged sections of the screen (Figure 17).

### Interface plugged-open

First we consider a model when two-thirds of the setup consists of a blank pipe (closed pores); the remaining one-third is occupied with a slotted screen (Figure 18). At low frequencies, a source in the middle of the blank pipe excites both fast and slow waves, as shown on Figure 18. The fast wave becomes highly attenuative upon reaching the interface. The slow wave experiences a strong reflection that is seen more easily on the wavefield-separated display (Figure 18).

At higher frequencies, fast-wave reflections become more observable. Modeling shows qualitatively similar behavior (Figure 19). First the fast wave becomes more attenuative in the open section. Second, although we observe both fast-fast and slow-slow reflections, the latter are substantially larger in amplitude, which is
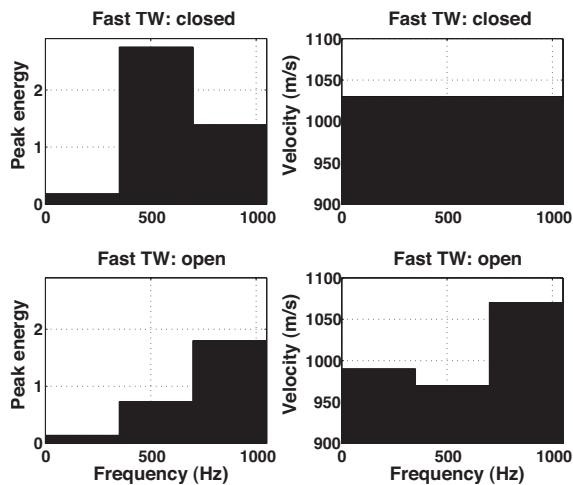


Figure 16. Distribution of energy (left) and peak velocity (right) of the fast tube wave for the synthetic data shown in Figure 14. To compare with the experimental data (Figure 12), we stack the energy within low-frequency (0- to 350-Hz), medium-frequency (350- to 700-Hz), and high-frequency (700- to 1050-Hz) bands. Note that in open pores, the fast tube wave is slowed at frequencies below 700 Hz and experiences anomalously strong attenuation in the medium-frequency range.
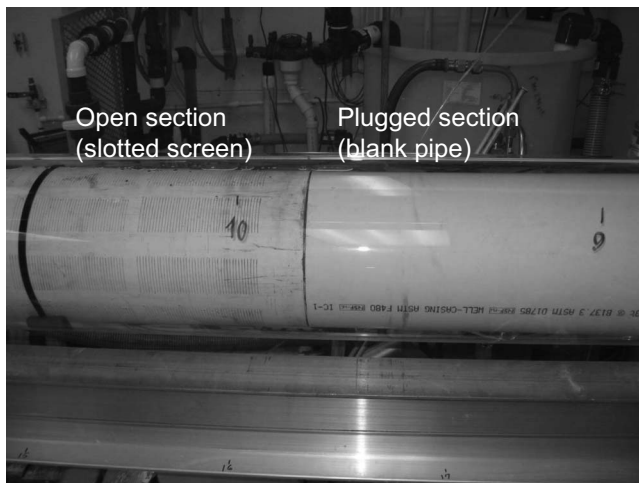


Figure 17. Connection between the slotted sand screen (left) and the blank PVC pipe (right) modeling an interface between open and closed pores. The outer glass pipe simulates casing.
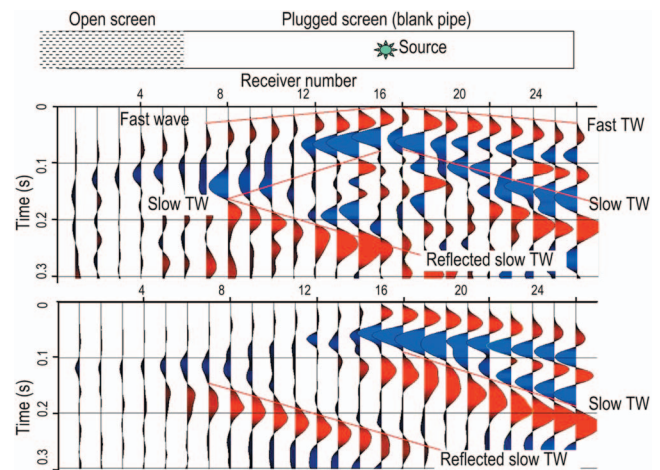


Figure 18. Experimental seismograms from a source with dominant frequency of 50 Hz show a reflection from a closed-open interface. Note the strong reflection of slow tube wave (∼300 m/s) from the interface. The fast tube wave has a velocity ∼1000 m/s. The top display shows raw data, whereas the bottom display shows a gather after median filtering (300 m/s) highlighting rightgoing slow tube waves.

consistent with the experimental data (compare Figure 18 and Figure 19). As before, we observe that modeling underestimates the amplitude of the slow wave in open pores.

### Interface open-plugged

When the source is inside the open section, wave propagation changes. First, at low frequencies, the slow tube wave dominating wave propagation in the open section converts into a fast wave in the plugged section (Figure 20). The interference between the strongly attenuating fast and slow waves creates the impression of a curved moveout around the source. However, it is clear that the fast wave is generated by a late-arriving direct slow wave. A simple inspection of the unprocessed gather reveals the location of the open-plugged interface where it manifests as the change in the slope of the dominant events.
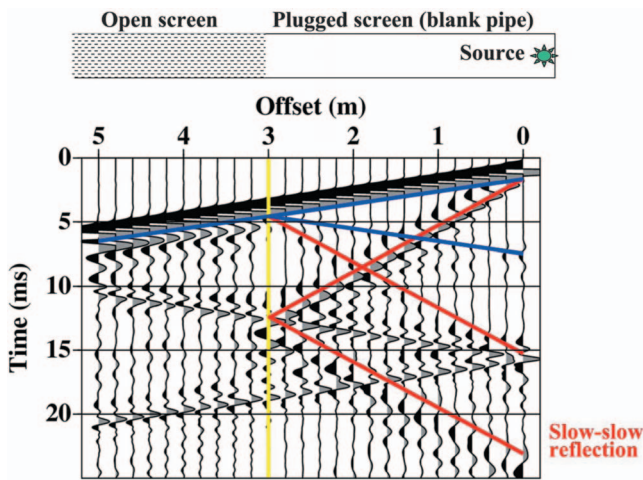


Figure 19. Synthetic seismograms from a source with central frequency of 1000 Hz in a model of an interface between closed- and open-to-flow sections of the screen. Parameters are as for version 2 of the glass setup from Table 2 and Table 3. Note that similar to experimental data in Figure 18, the direct slow wave (red line $\sim$280 m/s) causes the strongest reflection (slow-slow reflection), whereas the fast wave (blue line $\sim$1030 m/s) generates weaker fast- and slow-wave reflections. Unwanted reflections from model boundaries also are seen.
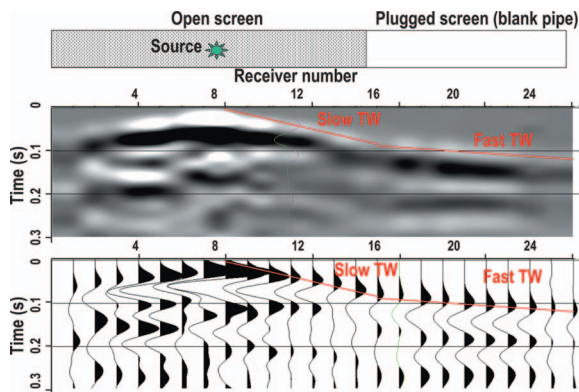


Figure 20. Experimental seismograms from a source with a dominant frequency of 50 Hz. The slow tube wave ($\sim$300 m/s) in the open section converts well into a fast wave ($\sim$1000 m/s) in the closed section. Top shaded display and bottom conventional wiggle view are displays of the same raw data.

Second, that same incident slow wave generates a strong reflection back into the open section (Figure 21) that is clearly larger than the earlier reflection from a pipe joint.

Third, at higher frequencies, we start to observe a direct fast wave from the source that quickly attenuates in the open section but then converts to a fast wave in the closed section, where it experiences less attenuation (Figure 22). Nevertheless, a stronger rightgoing fast wave is born, generated by conversion from a slow tube wave at later times.

### COMPLETION WITH A GRAVEL PACK: NUMERICAL MODELING

Let us analyze tube-wave signatures in gravel-packed completions, which are a subject of future experiments. To understand the influence of gravel sand on wave propagation, it is essential to properly predict the shear modulus of the sand. There are two possible scenarios:

1) If the shear modulus is small but nonvanishing, then the gravel pack is similar to a layer of a weak elastic material. The completion behaves as a composite (radially layered) poroelastic sur-
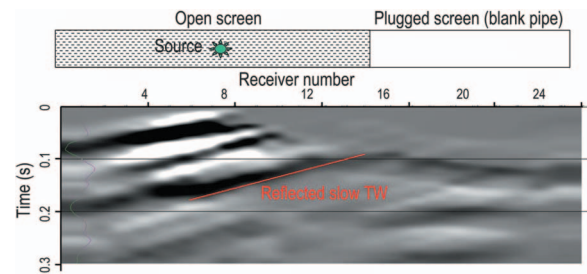


Figure 21. Experimental seismograms after median filtering with a velocity of 350 m/s highlighting leftgoing slow waves. The source has a dominant frequency of 100 Hz. A strong reflection for the slow tube wave ($\sim$300 m/s) is observed from the interface between the open and plugged sections.
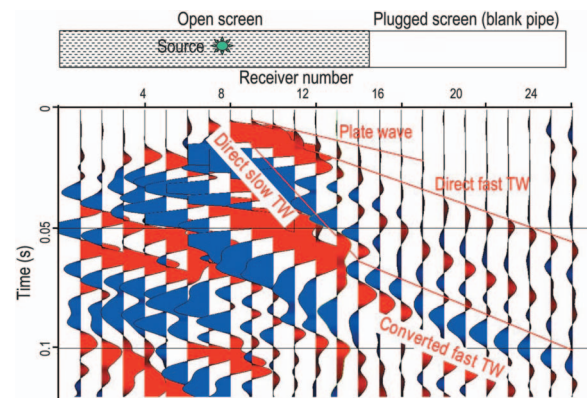


Figure 22. Experimental seismograms after median filtering with a velocity of 1050 m/s highlight rightgoing fast tube waves. The source dominant frequency is 500 Hz. At higher frequencies, we can see a direct fast wave from the source that continues as a fast wave in the plugged section. Nevertheless, we observe that the strongest fast wave is created by conversion from a slow tube wave later in time. Note that a plate wave ($\sim$1600 m/s) associated with the inner PVC pipe becomes visible near the source.

rounding consisting of a sand screen, gravel sand, and casing — all with a nonzero shear rigidity. If all layers are fully bonded, only a single tube wave exists.

2) If the shear modulus of sand is zero, then the gravel acts as a suspension and its behavior is similar to an effective high-density fluid but complicated by finite porosity and permeability. More than one tube wave would be observed in this case, making it similar to the case of a completion without a gravel pack.

We believe that in the normal case of good-quality gravel packs, the first scenario occurs. This is confirmed by visual inspection of gravel-packing procedures at the laboratory; once sand particles are

packed, they do not move with the flow but remain locked in place. That is indicative of grain-to-grain contact and nonvanishing shear rigidity.

The second scenario may occur in the case of fluidized sand when flow destabilizes the gravel pack (Wong et al., 2003) and grain-to-grain contact no longer takes place. Here we concentrate on the "normal" first scenario when the gravel pack is modeled as a poroelastic Biot medium with parameters given in Table 2. Shear-wave velocity remains the most uncertain parameter. For initial modeling, we have taken a value of 70 m/s, which lies between in situ estimates of ~120 to 150 m/s (Hamilton, 1976) and laboratory estimates of ~10 to 20 m/s from the method of Long et al. (2004).

In this section, we analyze wave propagation in the model describing the laboratory aluminum setup that would be used for an actual experiment with a gravel pack in the future. Thus, we examine a four-layer model with a free outer boundary consisting of fluid — inner pipe (screen) — sand — outer pipe (casing).

## Transmission signatures

If we neglect the poroelastic nature of the sand and the screen and model them as elastic impermeable media, then only two axisymmetric modes propagate at low frequencies (Figure 23):

1) T: tube wave supported by the composite pipe consisting of screen, sand, and casing
2) P: plate- or casing-type wave supported by the composite pipe

Thus, a gravel-packed completion has one-half the number of modes compared with a completion without gravel pack. This greatly simplifies wave propagation. The composite tube wave is closer in character to a fast tube wave and even maintains a similar velocity of ~1100 m/s. When sand becomes fluidized, a second (slow) tube wave emerges (Figure 23d), similar to the case of a completion without a gravel pack. Therefore, the presence of a second slow tube wave is diagnostic of completions with fluidized sand or lack of sand. The plate wave has a drastically lower velocity and becomes strongly dispersive because of highly contrasting elastic properties of the completion layers.

Finally, we note that additional axisymmetric modes appear at higher frequencies. Cutoff frequencies of the higher-order mode decrease with decreasing shear velocity of the sand (Figure 23). As a result, a very low shear velocity of the sand might create complex multimode wave propagation.

Synthetic seismograms (Figure 24) show that the tube wave dominates propagation at low frequencies, whereas the plate wave can be seen only with high amplification. In the plugged section of the screen (closed pores), the tube wave has a higher velocity and experiences very little attenuation, as expected. In contrast, open pores allow fluid communication between the liquid column inside the screen and pore fluid in the sand. As a result, we observe a strong velocity slowdown and dispersion as well as substantial attenuation, even at very short offsets. Thus, similar to open-hole logging meth-
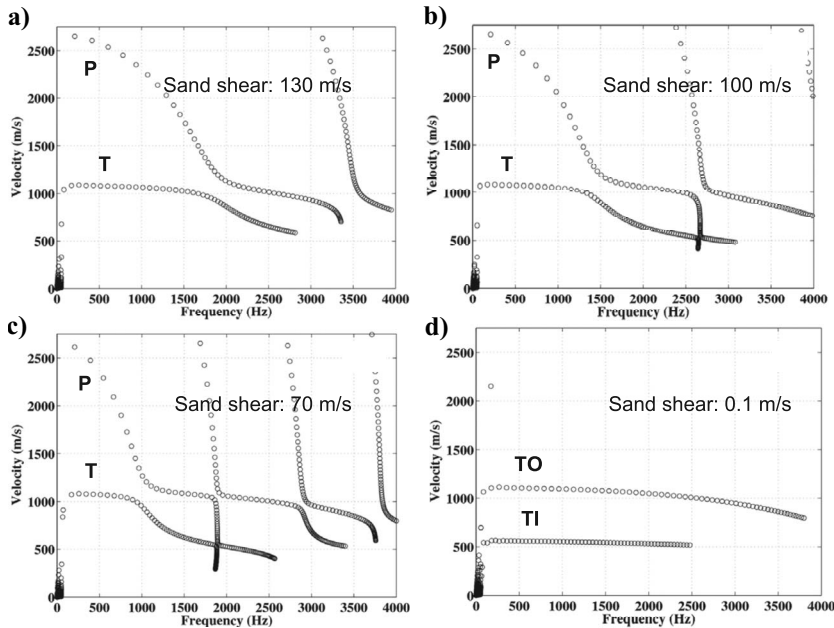


Figure 23. Dispersion curves for the four-layer laboratory model of a gravel-packed completion. Parameters are as for the aluminum setup from Table 2 and Table 3. The shear velocity of the sand is varied: (a) 130 m/s, (b) 100 m/s, (c) 70 m/s, and (d) 0.1 m/s. Note that a single tube wave T (~1100 m/s) and a single plate wave P (~2650 m/s) are the only two wave modes propagating at low frequencies for cases (a)-(c). Case (d) represents fluidized sand when a second (slow or inner TI) tube wave appears at 560 m/s. At very low frequencies, the algorithm produces unreliable values (Karpfinger et al., 2007).
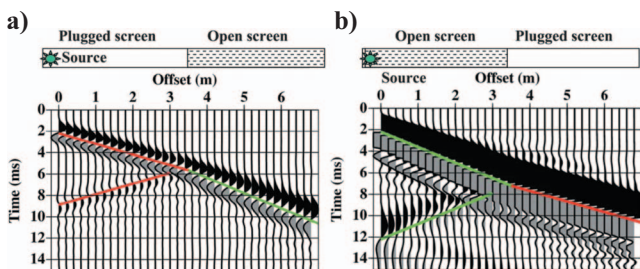


Figure 24. Finite-difference synthetic seismograms illustrate wave propagation and reflection-transmission in the laboratory model of gravel-packed completion (aluminum setup from Table 3). The central frequency of the source is 500 Hz. The sand screen and sand are modeled as poroelastic Biot layers with parameters from Table 2. The open-pore boundary condition between fluid and sand screen is set for open screens, whereas the closed-pore boundary condition simulates a plugged screen: (a) closed-open interface and (b) open-closed interface. In the plugged screen, the tube-wave velocity is ~1020 m/s (red lines), whereas in the open screen, it is ~700 m/s (green lines).

ods, we can distinguish permeable and impermeable sections of the screen by examining velocity and attenuation. Slowdown in velocity and high attenuation are simple diagnostics of an open section, whereas speedup and little or no attenuation are characteristics of a plugged section.

### Reflection signatures

Figure 24 also illustrates the reflection-transmission process at the plugged-open and open-plugged interface. Wave propagation is simplified compared with the case of no gravel pack because only a single tube wave is present in the open and plugged sections. The reflected tube wave results from the difference in velocities and attenuations across the interface. Interestingly, the reflection coefficient is large (~35%) for the closed-open interface, and it is small (~5%) for the open-plugged interface. Future experiments will aim to verify whether this asymmetric prediction is correct.

It is tempting to use a 1D effective-wavenumber approach (White, 1983; Tang and Cheng, 1993; Bakulin et al., 2005) to gain an insight into the physics of the reflection-transmission process. Although this approach was validated for poroelastic media (Bakulin et al., 2005) and radially inhomogeneous elastic media (Alexandrov et al., 2007), its validity for radially layered poroelastic media is yet to be established. In addition, it requires the ability to compute dispersion curves for layered poroelastic structures that is still the subject of research (Karpfinger et al., 2007). However, because of the 1D assumption, the effective wavenumber approach would predict that the reflection coefficients at plugged-open and open-plugged interfaces should be of the same magnitude and opposite sign, which contradicts the finite-difference modeling.

### FIBER-OPTIC IMPLEMENTATION

Laboratory experiment and modeling prove the concept of using tube-wave signals to monitor permeability changes along the completion. However, to implement this technique downhole, one needs to instrument producing wells with acoustic sources and receivers. Tools used in the laboratory are not applicable for real wells; downhole deployment requires these sources and receivers to be protected and not to obstruct the flow.

### Sensors

On the receiver side, such an objective is served well by fiber-optic sensors that could be placed on the outside of the pipe (sand screen, tubing, or casing). In addition, such sensors are completely passive and do not require electric power (Kirkendall and Dandridge, 2004). We tested this idea by comparing records obtained with hydrophones inside the plastic pipe and fiber-optic on-the-pipe sensors (Figure 25a). Good agreement is observed between the two sets of measurements (Figure 25b).

Inside the pipe, both tube and plate waves are described by a pistonlike motion at low frequencies. On the pipe wall, tube waves produce mainly radial displacement; plate waves produce mainly axial displacement (Lafleur and Shields, 1995). A fiber wrapped around the pipe detects the radial displacement of the pipe, which is characteristic of tube waves (often called "breathing" modes). In addition, azimuthal averaging performed by fiber-optic sensors tends to suppress other noises and highlight the axisymmetric tube wave.

The wrapping of fiber on the outside of the sand screen or casing is used with a real-time casing-imager (RTCI) tool (Rambow et al.,

2005; Childers et al., 2007), which aims to measure deformations of the pipe. RTCI sensors are finely spaced and wrapped in a continuous helical manner to detect asymmetric static deformations, whereas RTCM averages the circumference of the pipe at discrete locations but at a fine sampling interval in time.

There are opportunities to combine static and dynamic surveillance on the same fiber by using new interferometric technologies such as Blue ROSE, developed by the Naval Undersea Warfare Center for military security applications (Blackmon and Pollock, 2006). (Blue ROSE is the code name of the project; *Blue* refers to the blue color in the sky, which is caused by Rayleigh scattering, and *ROSE* is the acronym for Rayleigh optical scattering and encoding.) Blue ROSE technology detects Rayleigh backscattering profiles (or fingerprints) along the length of the fiber. Each segment of the optical fiber has a unique scattering profile resulting from random impurities in the fiber that cause Rayleigh scattering. The Blue ROSE system uses the Rayleigh fingerprints in the optical fiber as Fabry-Perot reflectors. The system can dynamically use different Rayleigh fingerprints anywhere along the length of the fiber. Blue ROSE gives a
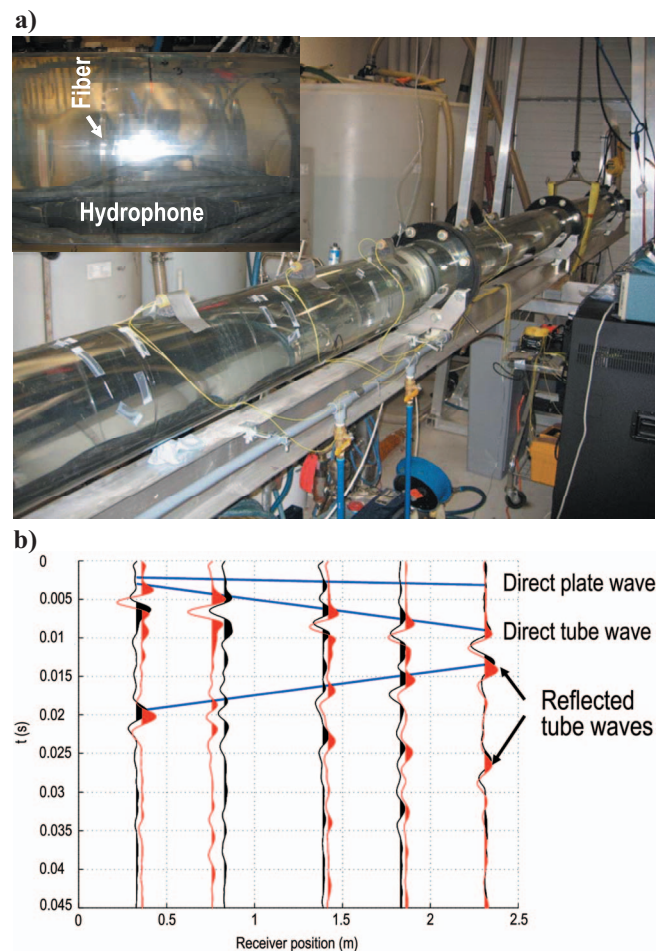
a)

b)

Figure 25. (a) Photograph of the flow-loop setup with fiber-optic sensors installed on the outside of the pipe. Conventional hydrophone sensors are present inside the fluid. (b) Comparison of traces recorded with hydrophones (black) and fiber-optic sensors (red). The source dominant frequency is 100 Hz. Note that the fiber-optic sensors suppress the plate wave with predominantly axial displacement because they are sensitive only to radial displacement of the pipe.

promise of combining both the RTCI and RTCM systems in a single cable, which would be desirable for complete downhole surveillance (Figure 26).

## Sources

Both transmission and reflection configurations of RTCM require repeatable excitation of the tube waves downhole. This can be achieved in two ways.

### Active sources

In principle, a dedicated active source can be clamped mechanically on the outside of the tubing or screen, similar to that cited in Ounadjela (2005), and can be mechanical or magnetostrictive (Etrema, 2007). Apart from additional installation in the well, this approach also requires electric power cable to supply the source.

### Passive noise sources

A less demanding alternative might be to use flow noise or other disturbances as a passive signal and to obtain the response between two sensors using crosscorrelation. So-called noise correlators have been used for decades to detect the location of subsurface leaks in the pipes (see Hunt, 2001, for a review). Lately, similar crosscorrelation of fiber-optic on-the pipe sensors has been used to measure tube-wave velocity and invert for fluid composition and flow speed in surface and downhole pipes (Gysling et al., 2002; Kragas et al., 2002). In the downhole case, the acoustic flowmeter contains an array of fiber-optic sensors installed on the outside of the tubing near the completion and performs acoustic measurements in real time while the well is flowing (Kragas et al., 2002). Successful use of acoustic flowmeters confirms the feasibility of downhole measurement of tube-wave velocity inside the producing and flowing well.

Crosscorrelation is a 1D version of the more general virtual-source method (Bakulin and Calvert, 2006). After crosscorrelation of a recording at the first receiver with those at the remaining sensors, we obtain a response as if the signal were emitted from a virtual source placed at the location of the first receiver. Because we directly measure the incident signal in the virtual source, we know the source signature and can modify it to our desired form by signal processing (Bakulin and Calvert, 2006). This is important for sensitive monitoring because it allows us to perform

- stacking of multiple records shaped with the same source signature to improve signal-to-noise ratio
- evaluation not only of velocity but also of attenuation of the tube-wave signals
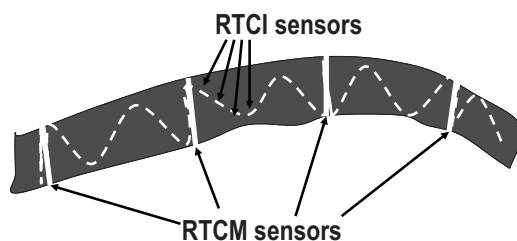


Figure 26. Schematic of combined RTCI and RTCM sensors on the same fiber using Blue ROSE interferometric technology.

Therefore, the virtual-source method might allow implementation of a completely passive version of RTCM without active sources downhole.

## CONCLUSIONS

We introduced real-time completion monitoring (RTCM), a new nonintrusive surveillance method that uses tube waves sent via the fluid column to identify permeability impairment in sand-screened completions. When the completion is entirely impermeable (plugged or impaired), tube-wave radial motion is resisted by elasticity of the completion layers that, along with fluid properties, determine tube-wave velocity and attenuation. When completion is open to flow, tube waves also can move borehole fluid back and forth radially across the permeable completion layers, and their velocity and attenuation become sensitive to radial permeability. Reduction in permeability resulting from sand-screen or perforation plugging or from near-wellbore impairment reduces well productivity and is detrimental to hydrocarbon production. Tube waves are capable of instant testing for the presence or absence of fluid communication across the completion and thus can allow identification of permeability change occurring in sand screens, gravel sand, perforations, and possibly in the reservoir.

We presented a proof-of-concept laboratory experiment verifying the method for a particular scenario in which impairment is caused by sand-screen plugging in completion without a gravel pack. In contrast to an open-hole scenario, we observed fast and slow tube waves supported by the casing and screen, respectively. Transmission experiments in open and plugged sand screens revealed substantially stronger attenuation of both tube waves in open or permeable sand screens. Low-frequency tube waves push borehole fluid back and forth radially through the sand screen, and this creates additional attenuation that is absent in the case of plugged or impermeable sand screens.

Modeling can explain observed differences if open screens are simulated as a highly permeable poroelastic Biot medium. Plugged screens can be simulated equally well by either elastic impermeable pipe or permeable pipe with no-flow boundary conditions at the interface. Although effective-medium poroelastic description is only a crude initial approximation for a complex sand screen, it appears to capture the two most important phenomena for tube-wave propagation: elastic resistance of the screen wall and inside permeability pathway for fluid exchange.

Fluid exchange through the permeable screen also creates anomalous attenuation of the fast tube wave in the medium-frequency range (300 to 600 Hz) observed in the experiment. Modeling replicates this effect and confirms that frequencies of the anomalous attenuation are controlled directly by hydraulic properties of the screen. With decreasing permeability, this anomalous band moves to higher frequencies. Therefore, this signature can be inverted directly for screen permeability.

Because velocity and attenuation are affected greatly by permeability, boundaries at which permeability changes should give rise to reflected and transmitted tube waves. Experiments validated this expectation with great success, thus providing an additional method of precise identification of permeability boundaries using reflected waves. In completions without gravel pack, the experimental effect of slow-wave conversion into fast wave at the open-plugged interface was particularly interesting.

Poroelastic modeling and experiment are in semiquantitative agreement with respect to the effects of screen permeability on fast tube-wave propagation and reflection. However, they disagree in explaining propagation and reflection-transmission of the slow tube wave in permeable screens. In particular, experimentation revealed a stronger, less dispersive slow tube wave in open screen that gives rise to a well-defined converted and reflected wave. In contrast, modeling predicted that the slow wave becomes a low-amplitude disturbance with extremely complicated dispersion and little reflection-transmission response. We believe poroelastic description of the permeable screens needs to be improved to reconcile these disagreements.

Further experiments are required to verify the effects of gravel sand and to measure the tube-wave signatures for other types of impairment to improve our ability to distinguish among different scenarios. Modeling suggests that the presence of gravel sand with nonzero shear rigidity leaves only a single composite tube-wave mode. Thus, the presence of a second tube wave is a direct diagnostic of a fluidized sand (with zero shear rigidity) or the lack of sand altogether. Tube-wave velocity of this single mode decreases and attenuation increases with increasing screen permeability.

Implementation of RTCM measurements downhole is likely to require protected and nonintrusive fiber-optic sensors to avoid obstruction to flow. We compared on-the-pipe fiber-optic sensors with hydrophones in the laboratory and found an excellent agreement. Although a downhole repeatable source is beneficial for acoustic monitoring, it might not be necessary. We anticipate that existing noise from flow can be used to excite tube waves, whereas crosscorrelation of traces at two receivers can produce a response between two points as if a virtual source has acted in one of the sensors. The ability to shape the virtual-source signal to a desired repeatable outcome is fundamental to achieving sensitive acoustic monitoring.

## ACKNOWLEDGMENTS

## APPENDIX A

## ZERO-FREQUENCY VELOCITIES IN MODELS WITH ONE AND TWO PIPES

First we provide expressions for a two-layer model of a fluid-filled pipe. Then we give equations for velocities in a four-layer model of two concentric elastic pipes filled with fluid. In both cases, the outer boundary of the pipe is considered to be traction free — a good ap-

proximation of the free-hanging pipe in the laboratory experiment. To illustrate that mode velocities are indeed related to either inner or outer pipes, we show decomposition of the four-layer model into a pair of two-layer models.

### Fluid-filled pipe (two-layer model)

A two-layer model of a fluid-filled pipe with a free outer boundary can be described by the following boundary conditions: vanishing tangential stresses on both sides of the pipe, zero normal stress on the outer side and continuity of radial displacement, and normal stress on the inner side of the pipe:

$$t_{rz}(r_0) = t_{rz}(r_1) = 0,$$
$$[t_{rr}(r_0)] = 0, \quad t_{rr}(r_1) = 0,$$
$$[u_r(r_0)] = 0, \tag{A-1}$$

where $r_0$ is the inner radius, $r_1$ is the outer radius of the pipe, and square brackets denote a jump of the corresponding quantity across the interface. Representing the wavefield inside each layer as a sum of outgoing and ingoing axisymmetric waves, these boundary conditions can be rewritten in a matrix form with a determinant forming a "characteristic" equation. The roots of the characteristic equation represent the velocities of all axisymmetric wave modes in such a model. At the zero-frequency limit, only two waves exist with velocities determined by a quadratic equation. The first wave is called a tube wave (White, 1983) because it represents a pistonlike motion of the fluid column resisted by the pipe. We call the second mode a plate wave because it is carried mainly by the pipe and has a velocity close to the wave speed of a fundamental axisymmetric mode in a free thin plate of the same material as the pipe.

The plate-wave velocity for a very thin pipe can be approximated by

$$C_{pl} = 2V_s \sqrt{1 - \frac{V_s^2}{V_p^2}}, \tag{A-2}$$

where $V_P$ and $V_S$ are longitudinal and shear velocities of the pipe material, respectively. Notably, the plate-wave velocity is not dependent on the properties of the fluid or the thickness of the pipe. In contrast, the tube-wave speed for a very thin and a very thick pipe can be approximated as

$$C_t = \frac{V_f}{\sqrt{1 + \frac{K}{\mu}\left[1 + \frac{2}{y(1 + \sigma)}\right]}}, \tag{A-3}$$

where $V_f$ is fluid acoustic velocity; $K$ is bulk modulus of the fluid; $\sigma$ and $\mu$ are the Poisson's ratio and the shear modulus of the pipe material, respectively; and

$$y = \frac{r_1^2}{r_0^2} - 1 \tag{A-4}$$

is a geometric parameter. Thus, tube-velocity depends on fluid and pipe elasticity as well as on the thickness of the pipe. Approximations A-3 can be found in White (1983) and in Henriet et al. (1983). In the case of a thick pipe ($y \gg 1$), equation A-3 produces a well-

known formula for the tube-wave velocity in a borehole surrounded by an infinite medium (White, 1983):

$$C_t^{(\infty)} = \frac{V_f}{\sqrt{1 + \dfrac{K}{\mu}}}. \qquad (A\text{-}5)$$

Equations A-2 and A-3 provide physical insight into the dependence of the wave speeds on model parameters and form a basis for inversion of material parameters from measured velocities.

Let us derive approximate expressions for velocities using the exact solution of the characteristic equation. At zero frequency, mode velocities $C = V_f/\sqrt{X}$ can be derived from the quadratic equation

$$EX^2 + FX + G = 0, \qquad (A\text{-}6)$$

with coefficients

$$E = 2y(1 + \sigma),$$
$$F = -4\gamma - 2y(1 + \sigma)(1 + \gamma) - y\beta,$$
$$G = 2\beta(1 - \sigma)\gamma + y\beta(1 + \gamma), \qquad (A\text{-}7)$$

where

$$\beta = \frac{V_f^2}{V_s^2},$$
$$\gamma = \beta\frac{\rho_f}{\rho} = \frac{K}{\mu}, \qquad (A\text{-}8)$$

with $\rho_f$ and $\rho$ being densities of fluid and pipe material, respectively. A somewhat more complex version of this equation can be found in Lafleur and Shields (1995).

It is convenient to introduce a parameter

$$B = -F - 2y\beta = 4\gamma + y[2(1 + \gamma)(1 + \sigma) - \beta] \qquad (A\text{-}9)$$

and to write the solutions as

$$X = \frac{B + 2y\beta \pm \sqrt{B^2 + 16y\beta\gamma\sigma^2}}{4y(1 + \sigma)}. \qquad (A\text{-}10)$$

In the following, we obtain engineering expressions A-2 and A-3 (velocities $C_t$ of tube and $C_{pl}$ of plate modes) as approximate solutions of equation A-6. If parameter $B$ is positive, then $C_t$ and $C_{pl}$ correspond to $X_+$ and $X_-$, respectively ($C_t = V_f/\sqrt{X_+}$, $C_{pl} = V_f/\sqrt{X_-}$). If parameter $B$ is negative, then $C_t$ and $C_{pl}$ correspond to $X_-$ and $X_+$ ($C_t = V_f/\sqrt{X_-}$, $C_{pl} = V_f/\sqrt{X_+}$). Therefore, when exact solutions A-10 are plotted as a function of model parameters and the sign of $B$ changes, then each curve (for either $X_+$ and $X_-$) describes not a single mode but a combination of the two modes, one for $B > 0$ and another for $B < 0$. Even though one must be careful in identifying the nature of the exact roots of equation A-6, approximate equation A-3 always tracks the mode supported mainly by the fluid column, whereas equation A-2 describes the mode supported mainly by the pipe.

Let us focus further discussion on the case when velocities from equations A-5 and A-14 satisfy the inequality $C_{pl}^{(\infty)} > C_t^{(\infty)}$. This is typical for many practical applications in which pipe material is usually "stiffer" than the fluid contained within the pipe. In this case,

$B > 4\gamma > 0$, and the square root in equation A-10 can be simplified by noticing that $B^2 \gg 16y\beta\gamma\sigma^2$ for the limits of thin ($y \ll 1$) and thick ($y \gg 1$) pipe. Therefore, the smaller second term under the square root can be omitted when we take the square root with "+" (plate wave) but should be left as a significant small number when we take the square root with "−" as B is subtracted (tube wave).

Finally, an approximation for the larger root provides the slow tube-wave velocity at thin- and thick-pipe limits

$$X_t \approx \frac{B + y\beta}{2y(1 + \sigma)} = 1 + \gamma + \frac{2\gamma}{y(1 + \sigma)}, \quad C_t = \frac{V_f}{\sqrt{X_t}}, \qquad (A\text{-}11)$$

whereas approximation for the smaller root gives the fast plate-wave speed

$$X_{pl} \approx \frac{B + 2y\beta - B\left[1 + \dfrac{8y\beta\gamma\sigma^2}{B^2}\right]}{4y(1 + \sigma)} = \frac{\beta\left[1 - \dfrac{4\gamma\sigma^2}{B}\right]}{2(1 + \sigma)}. \qquad (A\text{-}12)$$

For the thin-pipe limit, we have $B \to 4\gamma$ and

$$X_{pl}^{(0)} = \frac{\beta(1 - \sigma)}{2},$$
$$C_{pl}^{(0)} = \frac{V_f}{\sqrt{X_{pl}^{(0)}}} = \sqrt{\frac{Y}{\rho(1 - \sigma^2)}} = V_p\frac{\sqrt{1 - 2\sigma}}{1 - \sigma}. \qquad (A\text{-}13)$$

For the thick-pipe limit, we get $B \to \infty$ and

$$X_{pl}^{(\infty)} = \frac{\beta}{2(1 + \sigma)},$$
$$C_{pl}^{(\infty)} = \frac{V_f}{\sqrt{X_{pl}^{(\infty)}}} = \sqrt{\frac{Y}{\rho}} = V_p\sqrt{\frac{(1 - 2\sigma)(1 + \sigma)}{1 - \sigma}}. \qquad (A\text{-}14)$$

Note that thin- and thick-pipe limits for the plate-wave velocity are similar because

$$\frac{C_{pl}^{(\infty)}}{C_{pl}^{(0)}} = \sqrt{1 - \sigma^2},$$
$$0.85 < \frac{C_{pl}^{(\infty)}}{C_{pl}^{(0)}} < 1. \qquad (A\text{-}15)$$

It can be shown that under the assumptions made above ($C_{pl}^{(\infty)} > C_t^{(\infty)}$), plate-wave velocity for a finite thickness of the pipe is always bounded by the corresponding limits of equations A-13 and A-14 ($C_{pl}^{(\infty)} < C_{pl} < C_{pl}^{(0)}$). These bounds become narrower for materials with small Poisson's ratio.

### Two concentric pipes loaded with fluid (four-layer model)

Let us now consider a model of two concentric elastic pipes loaded with fluid. Motivated by the laboratory experiment, here we focus on the special case in which fluid that fills the interior of the smaller pipe and the annulus between pipes is identical. As before, the outer boundary of the larger pipe is considered to be traction free. Boundary conditions give us a characteristic equation of the fourth power that has four real roots corresponding to velocities of wave modes.

As explained in the main text, these are two pairs of plate and tube waves related to the outer and inner pipe, respectively. Although the exact equation can be solved for any frequency, a numerical solution provides little physical insight. Here we examine the characteristic equation at zero frequency and derive an approximate solution that allows us to understand the dependence of velocity for each mode on model parameters.

To obtain insightful approximations, it is useful to separate a four-layer model into a pair of independent two-layer subsystems: the first one (called inner) consists of the inner fluid-filled pipe, whereas the second one (called outer) comprises the outer pipe filled with the same fluid. Assuming that both subsystems have a traction-free outer boundary, each of them can be described by the characteristic equation considered above. Let us use the notations of the previous subsection without subscripts for the outer subsystem, whereas for the inner subsystem, we will add a subscript "$i$." For example, we write

$$\beta_i = \frac{V_f^2}{V_{si}^2}, \quad \gamma_i = \frac{\rho_f}{\rho_i}\beta_i, \quad E_i = 2y_i(1 + \sigma_i),$$

$$P_i(X) = E_i X^2 + F_i X + G_i = E_i(X - X_{ti})(X - X_{pli}),$$
$$(A\text{-}16)$$

where $V_{si}$ and $\rho_i$ are the shear velocity and density of the inner pipe and $X_{ti}$ and $X_{pli}$ are tube- and plate-wave speeds for the inner system.

The exact characteristic equation is the determinant of the matrix formed by boundary conditions for the four-layer system. Because the matrix has an almost blocky diagonal form at zero frequency, this equation can be presented as a product of equations for two independent subsystems with some additional terms associated with the nondiagonal elements of the matrix

$$P(X)P_i(X) - \theta E(X - 1)(X - X_{pl}^{(\infty)})P_i(X)$$
$$- 2\theta E(X - X_{pl}^{(\infty)})\gamma_i Q_i(X) = 0, \quad (A\text{-}17)$$

where

$$Q_i(X) = 2(X - 1)(X - X_{pli}^{(0)})$$
$$+ y_i(1 - \sigma_i)(X - \alpha_i)(X - 1 - \gamma_i), \quad (A\text{-}18)$$

and

$$X_{pl}^{(\infty)} = \frac{\beta}{2(1 + \sigma)}, \quad X_{pli}^{(0)} = \frac{\beta_i(1 - \sigma_i)}{2}, \quad \alpha_i = \frac{V_f^2}{V_{pi}^2},$$

$$\theta = \frac{r_{1i}^2}{r_0^2}. \quad (A\text{-}19)$$

Remarkably, this decomposition contains $X_{pl}^{(\infty)}$ and $X_{pli}^{(0)}$. These define the plate velocities of the outer pipe for thick-pipe limit (equation A-14) and the plate velocity of the inner pipe in the thin-pipe limit (equation A-13), respectively, whereas the term with $\alpha_i$ is controlled by the $P$-wave velocity of the inner pipe $V_{pi}$.

Additional or coupling terms in equation A-17 are proportional to the geometric factor $\theta$ that is the squared ratio of the outer radius of the smaller pipe to the inner radius of the larger pipe. When the annulus between the two pipes is large, then $r_{1i} \ll r_0$ and $\theta \to 0$. In this case, we can neglect additional terms in formula A-17 and obtain a factorized equation

$$P(X)P_i(X) = 0. \quad (A\text{-}20)$$

This means that our four-layer system can be decomposed into two independent two-layer subsystems.

Now let us devise another approximation valid for a nonzero $\theta$ when coupling between the two subsystems cannot be neglected. Let us rewrite the initial equation A-17 as

$$R(X)P_i(X) - 2\theta(X - X_{pl}^{(\infty)})\gamma_i Q_i(X) = 0, \quad (A\text{-}21)$$

where

$$R(X) = (X - X_t)(X - X_{pl}) - \theta(X - 1)(X - X_{pl}^{(\infty)}).$$
$$(A\text{-}22)$$

The plate-wave velocity for the outer pipe can be approximated well by the thick-pipe limit

$$X_{pl} \approx X_{pl}^{(\infty)}. \quad (A\text{-}23)$$

As a result, we separate the root that defines the outer plate wave, and by introducing

$$R_a(X) = (X - X_t) - \theta(X - 1), \quad (A\text{-}24)$$

we arrive at the approximate cubic equation for the remaining three velocities:

$$R_a(X)P_i(X) - 2\theta\gamma_i Q_i(X) = 0. \quad (A\text{-}25)$$

To achieve further factorization, we recall a useful approximation from the previous section, $X_{pli} \approx X_{pli}^{(0)}$. If, in addition, the Poisson ratio $\sigma_i$ is small ($\sigma_i < 0.2$), then we can introduce further approximation

$$X_{pli} \approx X_{pli}^{(0)} \approx \alpha_i, \quad (A\text{-}26)$$

which is verified easily by inspection of equation A-13.

Conditions A-26 allow us to further separate the second root defining the plate-wave velocity of the inner pipe and to obtain a quadratic equation for the two tube-wave velocities

$$R_a(X)y_i(1 + \sigma_i)(X - X_{ti}) - \theta\gamma_i[2(X - 1) + y_i(1 - \sigma_i)(X - 1 - \gamma_i)] = 0. \quad (A\text{-}27)$$

The exact solution of the last equation is

$$X_{\pm} = \frac{X_{ti}E_i(1 - \theta) + B_1 \pm \sqrt{B_1^2 + 2\theta(1 - \theta)\gamma_i E_i D}}{E_i(1 - \theta)},$$
$$(A\text{-}28)$$

where

$$B_1 = \frac{1}{2}E_i[X_t - \theta - X_{ti}(1 - \theta)] + \theta\gamma_i S,$$

$$D = 2\gamma_i + (X_{ti} - 1 - \gamma_i)S, \quad S = 2 + y_i(1 - \sigma_i).$$
$$(A\text{-}29)$$

At the limit of large annulus ($\theta \to 0$) and small annulus ($\theta \to 1$), we obtain, respectively (considering the case $C_t > C_{ti}$),

$$\theta = 0: \quad X_+ = X_{ti}, \quad C_+ = C_{ti}, \quad X_- = X_t, \quad C_- = C_t,$$

$$\theta \to 1: \quad X_+ \to \infty, \quad C_+ \to 0, \quad X_- = X_{ti} - \gamma_i \frac{D}{B_1},$$

$$C_- > C_{ti}. \tag{A-30}$$

Let us illustrate the use of these various approximations (Figure A-1). We take a base model from the second version of the experimental glass setup (Table 2 and Table 3) and vary a single parameter — the shear-wave velocity of the inner pipe. The plate-wave velocity related to the glass pipe is not shown because it remains almost fixed and independent of this parameter. Interestingly, blue and red exact dispersion curves (solid lines) approach, but instead of intersecting, they repulse each other at shear-wave velocity $\sim$600 m/s. Repulsion gives rise to an exchange of the wave character along the blue and red dispersion curves. For instance, below 600 m/s, the upper red curve corresponds to the outer tube wave, whereas above 600 m/s, it switches to the plate wave of the inner pipe.

Likewise, the blue curve switches from the inner plate wave to the outer tube wave when moving from low to high shear-wave velocities. The solutions for two independent subsystems (dashed lines) provide a good approximation for the velocities of the inner plate wave and of the outer tube wave but overestimate the speed of the slow inner tube wave. It is also remarkable that thin- and thick-pipe approximations for the inner plate-wave velocity (black dots) give a good description everywhere except near the repulsion point.

The solution of the approximate quadratic equation for the tube waves (green dots) provides an excellent description of the velocity of the inner tube wave, but it fails to predict the outer tube-wave ve-

locity at low shear-wave speeds. Such deterioration results from the fact that assumption A-26 becomes invalid for higher values of Poisson's ratio $\sigma_i$ or low values of $V_{si}$. Luckily, the largest root of equation A-27 (corresponding to the inner tube-wave velocity) remains accurate even for low $V_{si}$. This can be explained by reverting to cubic equation A-25. The largest root $X \to \infty$, determining the inner tube-wave slowness, depends only on the coefficients of the higher-order terms $X^3$ and $X^2$. Because these coefficients do not contain $\alpha_i$, the solution for this root remains accurate even when assumption A-26 is not met.

## REFERENCES

Alexandrov, D., B. M. Kashtan, A. Bakulin, and S. Ziatdinov, 2007, Tube-wave reflections in cased boreholes: 69th Annual Conference and Exhibition, EAGE, Extended Abstracts, P097.

Bakulin, A., and R. Calvert, 2006, The virtual source method: Theory and case study: Geophysics, **71**, no. 4, SI139–SI150.

Bakulin, A., B. Gurevich, R. Ciz, and S. Ziatdinov, 2005, Tube-wave reflection from a porous permeable layer with an idealized perforation: 75th Annual International Meeting, SEG, Expanded Abstracts, 332–335.

Biot, M. A., 1956, Theory of propagation of elastic waves in a fluid-saturated porous solid: Journal of the Acoustical Society of America, **28**, 168–191.

Blackmon, F., and J. Pollock, 2006, Blue Rose perimeter defense and security system: *in* E. M. Carapezza, ed., Sensors, and command, control, communications, and intelligence (C3I) technologies for homeland security and homeland defense V: Proceedings of the SPIE, 6201, 620123.

Chang, S. K., H. L. Liu, and D. L. Johnson, 1988, Low-frequency tube waves in permeable rocks: Geophysics, **53**, 519–527.

Childers, B. A., F. H. K. Rambow, D. E. Dria, M. Shuck, and S. Poland, 2007, Downhole fiber optic real-time casing monitor: Presented at the 14th Annual International Symposium on Smart Structures and Materials & Nondestructive Evaluation and Health Monitoring, SPIE Paper 6527-35.

Deresiewicz, H., and R. Skalak, 1963, On uniqueness in dynamic poroelasticity: Bulletin of the Seismological Society of America, **53**, 783–788.

Endo, T., 2006, Evaluation of formation permeability from borehole Stoneley waves: Journal of Geography, **115**, 383–399.

Etrema, 2007, http://www.etrema.com/cu18/, accessed November 5, 2007.

Gysling, D. L., A. D. Kersey, and J. D. Paduano, 2002, Fluid parameter measurement in pipes using acoustic pressures: US Patent 6 354 147.

Hamilton, E. L., 1976, Shear-wave velocity versus depth in marine sediments — A review: Geophysics, **41**, 985–996.

Henriet, J. P., J. Schittekat, and P. Heldens, 1983, Borehole seismic profiling and tube-wave applications in a dam site investigation: Geophysical Prospecting, **31**, 72–86.

Holzhausen, G. R., and R. P. Gooch, 1985, Impedance of hydraulic fractures: Its measurement and use for estimating fracture closure pressure and dimensions: SPE/DOE 13892, presented at SPE/DOE Low Permeability Gas Reservoirs Meeting.

Hunt, T. M., ed., 2001, Level, leakage and flow monitoring: Machine & System Condition Monitoring Series, Coxmoor Publishing Company.

Karpfinger, F., B. Gurevich, and A. Bakulin, 2007, Modeling of borehole modes using the spectral method: 69th Annual Conference and Exhibition, EAGE, Extended Abstracts, P095.

Kirkendall, C. K., and A. Dandridge, 2004, Overview of high performance fibre-optic sensing: Journal of Physics D: Applied Physics, **37**, R197–R216.

Kragas, T. K., F. X. Bostick III, C. Mayeu, D. L. Gysling, and A. van der Spek, 2002, Downhole fiber-optic multiphase flowmeter: Design, operating principle, and testing: Paper SPE 77655.

Lafleur, L. D., and F. D. Shields, 1995, Low-frequency propagation modes in a liquid-filled elastic tube waveguide: Journal of the Acoustical Society of America, **97**, 1435–1445.

Liu, H. L., and D. L. Johnson, 1997, Effects of an elastic membrane on tube waves in permeable formations: Journal of the Acoustical Society of America, **101**, 3322–3329.

Long, R., T. Vogt, M. Lowe, and P. Cawley, 2004, Measurement of acoustic properties of near-surface soils using an ultrasonic waveguide: Geophysics, **69**, 460–465.

Medlin, W. L., and D. P. Schmitt, 1994, Fracture diagnostics with tube-wave reflection logs: Journal of Petroleum Technology, **46**, no. 3, 239–248.

Ounadjela, A., 2005, Borehole acoustic source: US patent application 20050087391 A1.

Paige, R. W., L. R. Murray, and J. D. M. Roberts, 1995, Field application of hydraulic impedance testing for fracture measurement: SPE Production and Facilities, **10**, no. 1, 7–12.

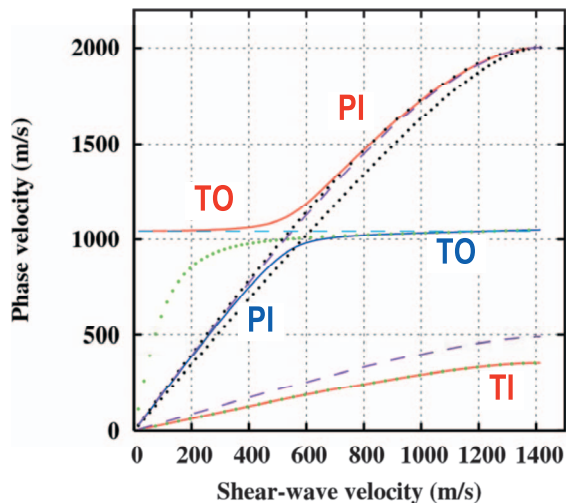Pourciau, R. D., J. H. Fisk, F. J. Descant, and R. B. Waltman, 2003, Comple-

Figure A-1. Zero-frequency velocities for the four-layer model as a function of shear-wave velocity in the inner pipe. Other parameters are taken from the second version of the glass setup (Table 2 and Table 3). Solid lines correspond to the exact solution of the characteristic equation for the four-layer system. Plate velocity for the outer pipe (PO) is not shown. Dashed lines are velocities for the two independent two-layer models represented by inner and outer pipes filled with water. Black dotted lines show thin-pipe (top line) and thick-pipe (bottom line) approximations for the plate-wave velocity of the inner pipe (equations A-13 and A-14). Green dotted lines (equation A-28) are exact solutions of the approximate quadratic equation A-27 for the fast and slow tube-wave velocities. Note characteristic repulsion of blue and red dispersion curves accompanied by the exchange of the wave character.

tion and well performance results, Genesis Field, deepwater Gulf of Mexico: Paper SPE 84415.

Rama Rao, V. N., and J. K. Vandiver, 1999, Acoustics of fluid-filled boreholes with pipe: Guided propagation and radiation: Journal of the Acoustical Society of America, **105**, 3057–3066.

Rambow, F. H. K., D. E. Dria, and D. R. Stewart, 2005, Apparatus and method for monitoring compaction: US patent N 6 854 327.

Rosenbaum, J. H., 1974, Synthetic microseismograms — Logging in porous formations: Geophysics, **39**, 14–32.

Sand Control, 2005, special supplement to World Oil: September, www.halliburton.com/public/pe/contents/Brochures/Web/H04505.pdf, accessed March, 31, 2006.

Schmitt, D. P., M. Bouchon, and G. Bonnet, 1988, Full-wave synthetic acoustic logs in radially semi-infinite saturated porous media: Geophysics, **53**, 807–823.

Tang, X. M., C. H. Cheng, and M. N. Toksöz, 1991, Dynamic permeability and borehole Stoneley waves: A simplified Biot-Rosenbaum model: Journal of Acoustical Society of America, **90**, 1632–1646.

Tang, X. M., and C. H. Cheng, 1993, Borehole Stoneley wave propagation across permeable fractures: Geophysical Prospecting, **41**, 165–187.

Tichelaar, B. W., H.-L. Liu, and D. L. Johnson, 1999, Modeling of borehole Stoneley waves in the presence of skin effects: Journal of the Acoustical Society of America, **105**, 601–609.

White, J. E., 1983, Underground sound — Application of seismic waves: Elsevier Science Publishing Company.

Winkler, K. W., H.-S. Liu, and D. L. Johnson, 1989, Permeability and borehole Stoneley waves: Comparison between experiment and theory: Geophysics, **54**, 66–75.

Wong, G. K., P. S. Fair, K. F. Bland, and R. S. Sherwood, 2003, Balancing act: Gulf of Mexico sand control completions, peak rate versus risk of sand control failure: Paper SPE 84497.

Ziatdinov, S., A. Bakulin, B. Kashtan, S. Golovina, and V. Korneev, 2005, Tube waves in producing wells with tubing and casing: 75th Annual International Meeting, SEG, Expanded Abstracts, 340–343.